



## Original Paper

# Insights into microscopic oil occurrence characteristics in shales from the Paleogene Funing Formation in Subei Basin, China



Jun-Jie Wang<sup>a</sup>, Peng-Fei Zhang<sup>a, b, \*</sup>, Shuang-Fang Lu<sup>a, c</sup>, Zi-Zhi Lin<sup>d</sup>, Wen-Biao Li<sup>a, c</sup>, Jun-Jian Zhang<sup>b</sup>, Wei-Zheng Gao<sup>a, b</sup>, Neng-Wu Zhou<sup>a, c</sup>, Guo-Hui Chen<sup>a, c</sup>, Ya-Jie Yin<sup>b</sup>, Han Wu<sup>b</sup>

<sup>a</sup> Sanya Offshore Oil & Gas Research Institute of Northeast Petroleum University, Sanya, 572025, Hainan, China

<sup>b</sup> College of Earth Science and Engineering, Shandong University of Science and Technology, Qingdao, 266590, Shandong, China

<sup>c</sup> Key Laboratory of Continental Shale Hydrocarbon Accumulation and Efficient Development, Ministry of Education, Northeast Petroleum University, Daqing, 163318, Heilongjiang, China

<sup>d</sup> School of Geoscience, China University of Petroleum (East China), Qingdao, 266580, Shandong, China

## ARTICLE INFO

## Article history:

Received 17 April 2024

Received in revised form

4 June 2024

Accepted 25 July 2024

Available online 29 July 2024

Edited by Jie Hao

## Keywords:

Occurrence characteristic

Shale oil content

Pore structure

Low-temperature nitrogen adsorption-desorption

Daqing, 163318, Heilongjiang, China

Guoyou Sag

## ABSTRACT

The microscopic occurrence characteristics primarily constrain the enrichment and mobility of shale oil. This study collected the lacustrine shales from the Palaeogene Funing Formation in the Gaoyou Sag, Subei Basin. Conventional and multistage Rock-Eval, scanning electron microscopy, and nuclear magnetic resonance (NMR)  $T_1$ – $T_2$  were performed to analyze the contents and occurrence characteristics of shale oil. Low-temperature nitrogen adsorption-desorption (LTNA/D) experiments were conducted on the shales before and after extraction. The relationships between shale oil occurrence with organic matter and pore structures were then discussed. Predominantly, the shale oil in the Funing Formation is found within fractures, with secondary occurrences in interparticle pores linked to brittle minerals and sizeable intraparticle pores associated with clay minerals. The selected shales can be categorized into two types based on the nitrogen isotherms. Type A shales are characterized by high contents of felsic and calcareous minerals but low clay minerals, with larger TOC and shale oil values. Conversely, Type B shales are marked by abundant clay minerals but diminished TOC and shale oil contents. The lower BET specific surface area (SSA), larger average pore diameter, and simpler pore surfaces and pore structures lead to the Type A shales being more conducive to shale oil enrichment and mobility. Shale oil content is predominantly governed by the abundance of organic matter, while an overabundance of organic matter typically equates to a reduced ratio of free oil and diminished fluidity. The BET SSA, volumes of pores less than 25 and 100 nm at extracted state all correlate negatively with total and adsorbed oil contents but display no correlation with free oil, while they have positive relationships with capillary-bound water. Consequently, pore water is mainly saturated in micropores (<25 nm) and minipores (25–100 nm), as well as adsorbed oil, while free oil, i.e., bound and movable oil, primarily exists in mesopores (100–1000 nm) and macropores (>1000 nm). These findings may enhance the understanding of the microscopic occurrence characteristics of shale oil and will contribute to guide resource estimation and shale oil sweet spot exploitation in the Gaoyou Sag, Subei Basin.

© 2025 The Authors. Publishing services by Elsevier B.V. on behalf of KeAi Communications Co. Ltd. This is an open access article under the CC BY-NC-ND license (<http://creativecommons.org/licenses/by-nc-nd/4.0/>).

## 1. Introduction

Enormous energy demand has increased attention on

unconventional oil and gas resources, especially shale oil resources (Jin et al., 2023). Unlike conventional oil and gas, sources and reservoirs are integrated for shale oil, meaning that shales are both source and reservoir rocks (Zou et al., 2020). Shale oil reservoirs are typified by high contents of clay minerals, plenty of nano-scale pores, low porosity, and extremely-low permeability, which restrict the distribution and mobility of shale oil (Li et al., 2020a; Ma

\* Corresponding author. Sanya Offshore Oil & Gas Research Institute, Northeast Petroleum University, Sanya, 572025, Hainan, China.

E-mail address: [zhangpengfei0907@sdust.edu.cn](mailto:zhangpengfei0907@sdust.edu.cn) (P.-F. Zhang).

et al., 2022; Wang et al., 2022a; Mei et al., 2023). Shale oil primarily includes adsorbed oil, adhering to pore surfaces or within kerogen, and free oil, mainly occurring in large inorganic pores or fractures (Li et al., 2017, 2018a, 2024; Dang et al., 2022). Free oil is further categorized into bound and movable oil, and movable oil is regarded as the primary contributor to shale oil production (Li et al., 2018a; Zhang et al., 2023b). Therefore, the characterization of shale oil occurrence has garnered significant scholarly interest.

Various technologies have been devised to analyze the content and microscopic occurrence characteristics of oil in shale. The chloroform asphalt “A” and  $S_1$  detected by Rock-Eval are prevalent metrics for gauging shale oil content (Lu et al., 2012; Zou et al., 2013; Wang et al., 2022b). The oil saturation index (OSI, defined as  $S_1/TOC$  or “A”/TOC) was introduced to assess the flowability of shale oil and has proven effective in identifying shale oil resource desserts (Jarvie, 2012; Li et al., 2015a; Zhang et al., 2022a). A higher OSI value corresponds to larger free oil content and better liquidity. Recently, multistage Rock-Eval has emerged as an innovative approach to detect shale oil in various states, such as total oil, adsorbed oil, and free oil contents (Jiang et al., 2016; Cao et al., 2023). Combined with multistage Rock-Eval, a suite of equations has been formulated to determine the adsorbed and free oil contents, utilizing the  $S_1$  and  $S_2$  parameters from conventional Rock-Eval (Zhang et al., 2022b). Scanning electron microscopy (SEM) can visually display the microscopic occurrence characteristics of shale oil (Zhang et al., 2023c). Specifically, adsorbed oil mainly exists on the surface of organic matter or minerals, such as pyrite aggregates, whereas free oil predominantly occupies the central regions of pores or fractures.

Furthermore, the elucidation of residual shale oil occurrence pore sizes is achievable through the comparative analysis of pore size distributions (PSDs) derived from low-temperature nitrogen adsorption-desorption (LTNA/D) and mercury intrusion capillary pressure (MICP) before and after extraction (Wang et al., 2019; Bai et al., 2022; Zhang et al., 2023c; Lin et al., 2024). The previous study indicated that the residual shale oil mainly occurred in the pores less than 100 nm in the Dongying Sag, Bohai Bay Basin, with the lower pore size thresholds for free and movable oil being approximately 5 and 30 nm, respectively (Wang et al., 2019). Contrastingly, the lower limit of pore size for free oil in the Qingshankou Formation is about 10 nm (Bai et al., 2022). The occurrence pore sizes of residual shale oil in adsorbed and free states can be discerned by integrating multi-step extraction with LTNA/D methodologies (Lin et al., 2024). Furthermore, the dean-stark extraction technique has been employed to quantify the contents of pore water and oil within shales (Li et al., 2022a).

Low-field nuclear magnetic resonance (NMR)  $T_1$ – $T_2$  serves as an alternative technique to assess the occurrence characteristics of shale pore fluids. The NMR  $T_1$ – $T_2$  can be classified into distinct regions according to the values of  $T_2$  and  $T_1/T_2$ , and several NMR  $T_1$ – $T_2$  patterns for shales have been proposed (Li et al., 2018b; Wang et al., 2024; Zhang et al., 2020). These patterns facilitate the effective identification of kerogen, capillary-bound water, adsorbed oil, and free oil. The amplitudes of these regions can be quantitatively ascertained, exhibiting congruence with the results from TOC and Rock-Eval analyses (Liu et al., 2019, 2022; Li et al., 2020b). Post-calibration of amplitude, the different types of pore fluids in shale, such as capillary-bound water, adsorbed oil, and free oil, can be quantitatively determined (Zhang et al., 2023c). Given that the  $T_2$  value theoretically correlates with pore size, the occurrence pore sizes of various fluid types can be inferred from the  $T_1$ – $T_2$  spectrum (Zhang et al., 2022a, 2023b).

The microscopic occurrence of shale oil is constrained by various factors. Organic matter primarily controls the contents and occurrence of shale oil (Wang et al., 2015, 2022a; Guan et al., 2022; Wang

et al., 2022c). A larger content of organic matter generally leads to a larger shale oil content but a higher adsorbed oil, corresponding to a lower free oil ratio or OSI (Wang et al., 2015; Zhang et al., 2021). Additionally, the type and maturity of organic matter exert a significant influence on adsorbed oil, particularly adsorbed oil (Guan et al., 2022). The shale oil occurrence is also affected by inorganic minerals, with clay minerals, for instance, providing extensive specific surface areas that impact the prevalence of adsorbed oil (Zhang et al., 2023c). The pore systems, serving as reservoirs for shale oil, directly govern its micro-occurrence (Liang et al., 2022). The Brunauer-Emmett-Teller (BET) specific surface area (SSA) is positively associated with adsorbed oil content, while a larger average pore diameter is indicative of increased total oil and free oil contents.

This study endeavors to dissect the microscopic occurrence of shale oil and its influencing factors in the Funing Formation in Gaoyou Sag, Subei Basin, China. A comprehensive suite of analyses, including TOC, conventional and multistage Rock-Eval, SEM, and NMR  $T_1$ – $T_2$ , were executed to ascertain the shale oil contents and occurrence characteristics. LTNA/D experiments were performed on the shales before and after extraction to disclose the occurrence pore sizes of shale oil. Finally, the influences of organic matter and pore structure on shale oil occurrence were discussed. The findings proffer valuable insights into the shale oil occurrence and its controlling factors in the Gaoyou Sag, Subei Basin.

## 2. Experiments and methods

### 2.1. Geological setting

The Subei Basin, situated in the northern part of the Lower Yangtze Block and considered the onshore component of the Subei-South Yellow Sea Basin, is a continental fault basin that evolved through the Late Cretaceous and continued into the Mesozoic and Cenozoic eras (Duan et al., 2020). It extends north to the Lusu Uplift, south to the Sunan Uplift, and is connected to the South Yellow Sea in the east, with an area of about  $3.5 \times 10^4$  km<sup>2</sup>, including two depressions, Yanfu and Dongtai Depressions, and Jianhu Uplift (Fig. 1(a)) (Fu et al., 2020). Gaoyou Sag, positioned centrally within the Dongtai Depression, emerges as the focal point for shale oil exploration area in the Subei Basin. The Subei Basin has undergone four distinct evolutionary phases: Late Cretaceous faulting, subsidence during the Paleogene, fault-induced subsidence in the Eocene, and thermal subsidence throughout the Neogene and Quaternary. These processes have led to the deposition of the Taizhou ( $K_2t$ ), Funing ( $E_1f$ ), Dainan ( $E_2d$ ), Sanduo ( $E_2s$ ), Yancheng ( $N_2y$ ), and Dongtai (Qd) Formations in ascending order (Liu et al., 2020; Zan, 2020). The Funing Formation was deposited during the first main rifting period (83–54.9 Ma), consisting of four members ( $E_1f_1$  to  $E_1f_4$ ) from bottom to top. The second member of the Funing Formation ( $E_1f_2$ ) was deposited in a semi-deep to deep lake environment, characterized by the extensive development of dark gray shales and mudstones. The  $E_1f_2$  member is further divided into five shale layers, denoted as Sub-members I to V, as shown in Fig. 1(b) and (c). The  $E_1f_2$  is the primary objective for shale oil exploration, where significant breakthroughs have been achieved (Zhu et al., 2023).

### 2.2. Samples and experiments

#### 2.2.1. Samples

This study collected 24 shale samples from the Paleogene Funing Formation in the Gaoyou Sag, Subei Basin. Shale samples were collected from two wells (Y1 and Y2) in the Gaoyou Sag (Fig. 1(a)). Specifically, samples TY1–TY9 were extracted from Well Y1 in the

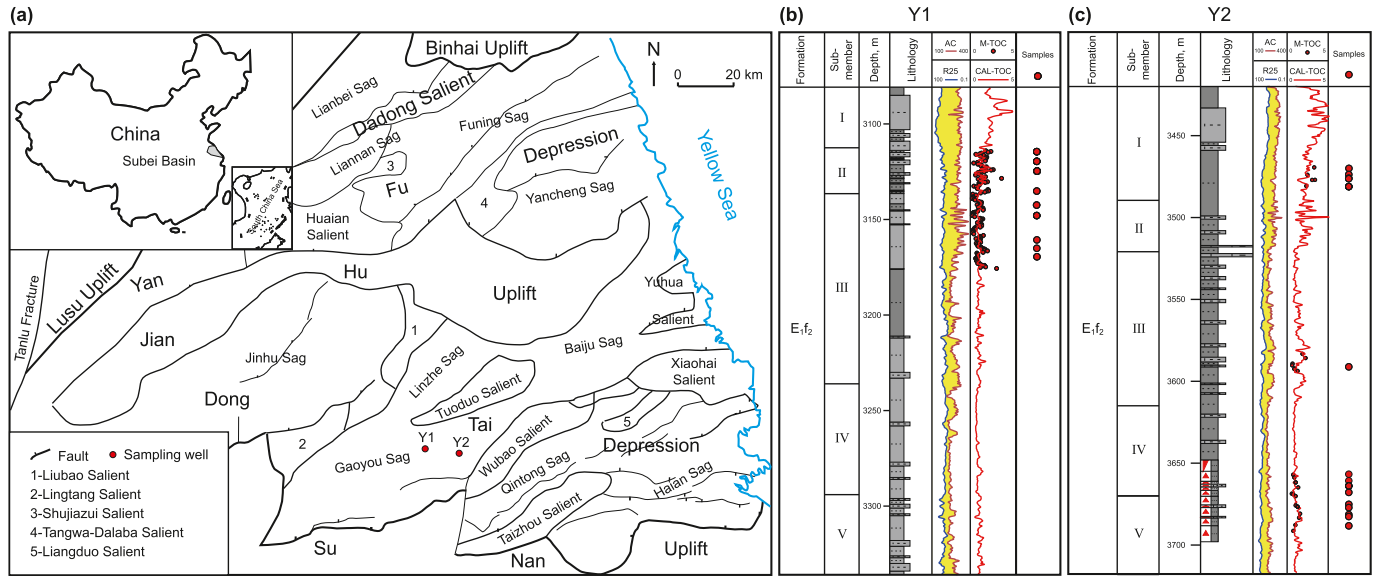


**Fig. 1.** Geological setting of the Subei Basin (a) and sample location ((b) and (c)) (Zhang et al., 2022b, 2023c). M-TOC refers to the measured TOC values; Cal-TOC represents the TOC calculated by well logs.

Sub-members II and III, and samples TY10–TY24 originated from the Sub-members I, III, IV, and V in Well Y2. A range of experiments were performed to analyze the shale oil occurrence characteristics and controlling factors, such as TOC, X-ray diffraction (XRD), Rock-Eval, SEM, LTNA/D, and NMR  $T_1$ – $T_2$ .

2.2.2. TOC and Rock-Eval

The TOC and Rock-Eval were first conducted on the as-received (AR, i.e., unextracted) shales. The unextracted shales underwent a thorough cleansing process using a mixed solution of dichloromethane and acetone (3:1 in volume) at 80 °C and 0.2 MPa for 7 d, followed by a drying phase in a vacuum oven set at 110 °C for 24 h. The conventional Rock-Eval tests were performed on the extracted shales. A LECO-CS230 instrument was used to determine the TOC values of shale followed by the national standard of P.R.C. (GB/T 19145-2022 Determination for total organic carbon in sedimentary rock). The conventional and multistage Rock-Eval were conducted on a Rock-Eval VI instrument according to the standard of GB/T 18602-2012 (Rock pyrolysis analysis). The conventional Rock-Eval includes two steps: initially maintaining a steady temperature of 300 °C for 3 min to procure the  $S_1$ , subsequently escalating to 600 °C at a rate of 25 °C/min to ascertain the  $S_2$ . However, the multistage Rock-Eval consists of four steps.  $S_{1-1}$  was first tested at a temperature of 200 °C for 1 min, and then  $S_{1-2}$  was obtained as the temperature increased to 350 °C at a rate of 25 °C/min and remained for 1 min. The temperature continued to ascend to 450 °C at the same rate, maintained for 1 min to quantify  $S_{2-1}$ . The final stage involved identifying the  $S_{2-2}$  with the temperature climbing to 600 °C at a consistent rate.  $S_{1-1}$  and  $S_{1-2}$  are indicative of free oil, while  $S_{2-1}$  represents adsorbed oil (Jiang et al., 2016). The methodologies pertaining to TOC and Rock-Eval testing are elaborated in the authors' preceding study (Zhang et al., 2022b).

2.2.3. LTNA/D

The LTNA/D measurements were conducted on the unextracted and extracted shales. The unextracted shale samples were first pulverized into a fine powder (40–60 mesh). These samples were then subjected to desiccation in a vacuum oven at 60 °C for 6 h, and then the LTNA/D measurements were conducted. Subsequently, the powdered samples underwent an oil-washing procedure and were

dried employing the aforementioned method. After drying at 110 °C under vacuum conditions for 6 h, the LTNA/D measurements on extracted shales were carried out. According to the standard of GB/T 21650.2-2008, this study conducted LTNA/D experiments on a Micromeritics ASAP 2460 surface area and porosity analyzer. The adsorption and desorption isotherms were recorded over a  $P/P_0$  ranging from 0.01 to 0.993 at 77 K. The SSA was computed utilizing the BET model, while the PSD was ascertained via the BJH method.

2.2.4. SEM and NMR  $T_1$ – $T_2$

To elucidate the microscopic occurrence characteristics of shale oil, SEM experiments were performed on the unextracted shales. The thin shale sections were first hand-polished on stubs and then polished by argon-ion milling to obtain a flat surface. A Phenom Prox scanning electron microscope was used to observe shale pore-fracture micro-distributions without coating, and a series of back-scattered electron (BSE) images were obtained with magnification ranging from 400 to 6000 (Zhang et al., 2023c). The methodology for identifying oil within pores and associated with minerals, such as quartz, feldspar, pyrite, calcareous, and clay minerals, has been comprehensively described in extant literature (Zhang et al., 2023c).

The NMR  $T_1$ – $T_2$  spectrum was acquired from a MesoMR23-060H-I spectrometer, operating at a resonance frequency of 21.36 MHz within a low magnetic field of 0.52 T. The IR-CPMG (Inversion Recovery-Carr-Purcell-Meiboom-Gill) sequence was used to collect the  $T_1$ – $T_2$  spectrum, and the sequence parameters were set as: TW (Waiting time) = 3000 ms, TE (echo time) = 0.07 ms, NS (number of scans) = 32, NECH (echo number) = 6000, and NTI (number of Inverse Time) = 25, as discussed in the previous study (Zhang et al., 2020). The NMR  $T_1$ – $T_2$  spectra of the selected shales at unextracted (AR) state were detected.

3. Results and discussion

3.1. Characteristics of selected shales

3.1.1. Organic geochemical characteristics

The tabulated data in Table 1 encapsulates the TOC contents and conventional Rock-Eval parameters for unextracted and extracted

**Table 1**  
TOC and conventional Rock-Eval parameters of the unextracted and extracted shales.

Sample	Depth, m	Unextracted					Extracted		
		TOC, wt.%	S <sub>1</sub> , mg/g	S <sub>2</sub> , mg/g	T <sub>max</sub> , °C	HI, mg/g	S <sub>1</sub> <sup>*</sup> , mg/g	S <sub>2</sub> <sup>*</sup> , mg/g	T <sub>max</sub> <sup>*</sup> , °C
TY1	3114.57	1.33	2.24	2.85	396	214	0.16	0.79	426
TY2	3119.55	1.10	1.11	2.26	380	205	0.11	0.57	398
TY3	3124.59	1.52	1.07	1.80	380	119	0.19	0.81	395
TY4	3134.52	1.55	1.38	2.71	388	175	0.16	0.61	386
TY5	3144.51	1.32	2.67	3.13	408	238	0.09	0.52	412
TY6	3149.11	0.79	1.19	1.92	409	244	0.11	0.56	438
TY7	3160.55	0.85	1.19	2.36	411	278	0.12	0.71	423
TY8	3164.56	0.86	0.71	1.34	383	157	0.17	0.62	411
TY9	3169.73	0.51	0.45	1.12	416	219	0.10	0.49	421
TY10	3469.55	3.31	2.92	14.71	449	445	0.12	11.23	447
TY11	3474.05	2.46	2.88	12.13	451	493	0.10	8.05	449
TY12	3477.10	3.41	2.65	15.43	446	452	0.18	12.17	449
TY13	3477.15	3.05	2.88	13.14	448	431	0.16	9.57	448
TY14	3480.80	2.40	2.12	9.04	447	377	0.12	6.02	447
TY15	3591.51	0.80	1.61	2.57	440	321	0.06	0.61	441
TY16	3655.20	0.96	1.46	1.65	428	172	0.03	0.33	437
TY17	3663.20	1.29	0.77	3.51	443	272	0.05	1.69	451
TY18	3668.50	0.97	0.99	2.13	434	220	0.06	0.61	442
TY19	3676.81	1.53	1.09	5.35	444	350	0.09	2.41	447
TY20	3681.10	1.29	0.81	2.80	432	217	0.08	0.84	442
TY21	3682.80	2.20	0.85	8.50	443	386	0.03	6.26	447
TY22	3684.20	1.20	0.78	2.59	435	217	0.07	0.81	437
TY23	3685.96	0.94	1.01	2.21	427	236	0.07	0.61	439
TY24	3691.96	0.97	0.72	1.80	436	185	0.11	0.65	434

shales. The TOC contents are between 0.51% and 3.41%, with an average of 1.53%. The S<sub>1</sub> at unextracted state fluctuates between 0.45 and 2.92 mg/g, with a mean of 1.48 mg/g, whereas the S<sub>2</sub> values range from 1.12 to 15.43 mg/g, averaging 4.88 mg/g. The T<sub>max</sub> averages of 424 °C (380–451 °C) and the hydrogen index (HI) oscillates between 119 and 493 mg/g, indicating that the organic matter types include Types I, II<sub>1</sub>, and II<sub>2</sub>, as shown in Fig. 2. After extraction, a marked decrease in S<sub>1</sub><sup>\*</sup> is observed, averaging at 0.11 mg/g (0.03–0.19 mg/g), significantly lower than the unextracted S<sub>1</sub> average of 1.48 mg/g. Concurrently, S<sub>2</sub><sup>\*</sup> values also exhibit a notable reduction, with a mean of 2.81 mg/g (0.33–12.17 mg/g). In contrast, the T<sub>max</sub><sup>\*</sup> increases to an average of 432 °C (386–451 °C), aligning with findings from the previous research (Bai et al., 2022; Zhang et al., 2023c). The volatilization temperature of residual oil is lower than the pyrolysis temperature of solid kerogen. Hence, the extraction process results in the removal of residual oil, and the elevated pyrolysis temperature of solid kerogen contributes to the increased T<sub>max</sub> (Zhang et al., 2023d).

### 3.1.2. Mineral compositions

The mineral compositions of the examined shales are intricate, predominantly comprising quartz, feldspar, calcite, dolomite, and clay minerals, as delineated in Table 2 and illustrated in Fig. 3(a). Quartz emerges as the most abundant constituent, averaging 27.7% and ranging from 8.6% to 44.0%, followed by the clay minerals, varying from 5.7% to 59.51%, with a mean of 24.4%. The dolomite has an average content of 21.0% (1.3%–68.9%), while calcite is between 1.7% and 42.8% (mean 12.6%). Felspar maintains an average of 12.6% (2.6%–27.3%). Additionally, minor quantities of orthoclase (average 2.2%) and pyrite (average 1.8%) are present. The lithological classification of the selected shales was ascertained based on the tripartite elemental composition of felsic, calcareous, and clay minerals. The prevalence of lithologies is in the order of felsic-rich, followed by felsic, calcareous-rich, and calcareous shales, as depicted in Fig. 3(b). The argillaceous and argillaceous-rich shales are less common, attributable to their minimal clay mineral content. As discussed in the previous study (Zhang et al., 2023c), the shales with a total organic carbon (TOC) exceeding 1.5% are classified as organic-rich. However, all six types of lithologies develop organic-rich shales (Fig. 3(b)), implying that all lithological shales may be enriched in shale oil. Consequently, it is inferred that the TOC contents and pore structures may be pivotal in governing shale oil enrichment.

## 3.2. Shale oil contents and occurrence characteristics

### 3.2.1. Shale oil contents

Multistage Rock-Eval serves as a robust methodology for the quantification of shale oil content. The multistage Rock-Eval parameters of the selected shales are enumerated in Table 3. The light oil, denoted as S<sub>1-1</sub>, exhibits relatively low values, averaging at 0.11 mg/g (ranging from 0.04 to 0.25 mg/g), attributable to the pre-testing evaporation of most light oil constituents (Zhang et al., 2022b). The S<sub>1-2</sub> parameter, representing light to medium oil, spans from 0.80 to 3.43 mg/g, with an average of 1.98 mg/g, while the adsorbed oil (S<sub>2-1</sub>) varies between 0.79 and 5.64 mg/g (average 2.37 mg/g). Moreover, the kerogen pyrolysis hydrocarbons,

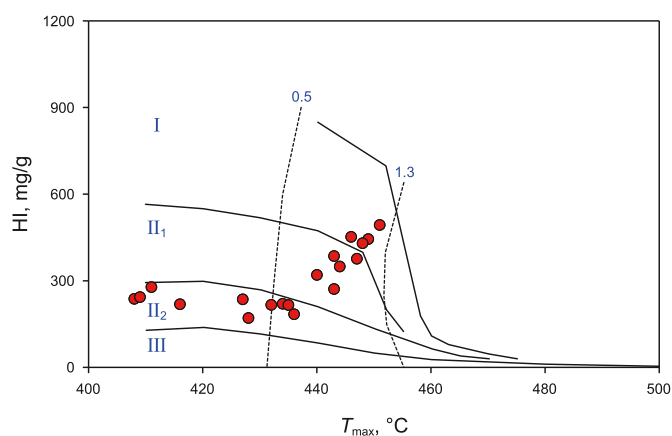


**Fig. 2.** Relationship between HI and T<sub>max</sub> of the selected shales before extraction.

**Table 2**  
Mineral compositions of the studied shales.

Sample	Lithology	Mineral composition, wt.%						
		Quartz	Orthoclase	Feldspar	Calcite	Dolomite	Pyrite	Clay mineral
TY1	B3	20.0	1.0	4.4	4.5	37.6	1.1	29.8
TY2	B2	24.8	/	6.2	13.1	8.5	1.5	45.9
TY3	A2	26.8	/	4.7	2.9	4.2	1.9	59.5
TY4	B2	24.3	/	4.9	/	21.7	1.3	47.8
TY5	A3	13.3	/	2.6	3.3	54.3	1.1	24.0
TY6	A1	38.7	4.0	16.8	2.7	3.6	1.0	28.1
TY7	B3	17.7	/	5.6	11.9	24.5	1.2	30.2
TY8	B1	29.0	/	8.5	2.7	12.7	1.2	29.9
TY9	A3	11.9	/	4.6	5.8	44.5	1.1	23.2
TY10	A1	38.8	/	11.3	1.8	30.4	2.4	15.3
TY11	B1	37.8	/	5.6	40.1	1.3	1.8	13.3
TY12	A1	41.9	/	6.6	27.8	/	2.0	20.0
TY13	A1	44.0	/	11.2	19.4	/	3.0	18.7
TY14	A1	35.5	/	23.4	10.3	/	3.0	26.7
TY15	A1	38.7	3.6	23.7	7.3	8.6	1.5	16.6
TY16	A1	24.5	3.8	23.7	14.3	17.6	1.6	13.9
TY17	A3	11.6	/	5.8	6.1	68.9	1.9	5.7
TY18	A1	34.8	2.4	18.8	8.6	9.6	2.0	22.9
TY19	B3	22.2	0.5	16.6	37.0	6.1	2.5	15.1
TY20	B1	31.5	1.7	11.7	1.7	19.8	2.2	31.4
TY21	A3	8.6	/	27.3	42.8	11.8	2.5	7.1
TY22	A1	34.3	2.2	24.6	7.3	12.1	2.6	16.5
TY23	B1	25.9	/	21.5	3.9	26.4	2.1	19.7
TY24	B1	27.4	1.1	13.1	15.4	17.7	2.0	23.2

A1, A2, and A3 refer to the felsic-rich, argillaceous-rich, and calcareous-rich shales; B1, B2, and B3 represent the felsic, argillaceous, and calcareous shales; the symbol “/” indicates that it has not been detected.

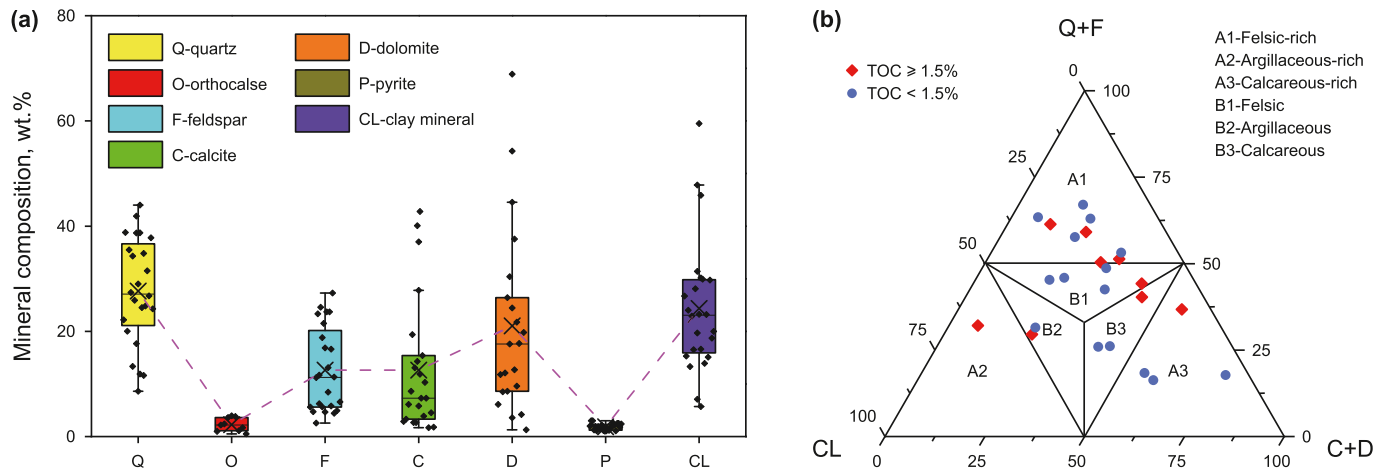


**Fig. 3.** Mineral compositions (a) and lithologies (b) of the selected shales.

reflected by  $S_{2-2}$ , average 2.85 mg/g (0.12–11.14 mg/g). As a result, the free oil ( $S_F$ ) can be computed as the aggregate of  $S_{1-1}$  and  $S_{1-2}$ , ranging from 0.84 to 3.64 mg/g (average 2.09 mg/g). The total oil content ( $S_{T1}$ ), encompassing both free and adsorbed oil, spans from 1.63 to 9.26 mg/g, averaging 4.46 mg/g.

As discussed,  $S_1$ , originated from conventional Rock-Eval, typically omits light and heavy hydrocarbons, with the latter being detected within the  $S_2$  (Xue et al., 2016). Disregarding the depletion of light hydrocarbons implies that residual shale oil is composed of  $S_1$  and heavy hydrocarbons. Therefore, the total residual shale oil contents can be ascertainable through the juxtaposition of conventional Rock-Eval outcomes between unextracted and extracted states (Jarvie, 2012). The total oil content is the difference in conventional pyrolysis parameters before and after extraction, i.e.,  $S_{T2} = (S_1+S_2) - (S_1^*+S_2^*)$ . As determined by conventional Rock-Eval, this total oil content ( $S_{T2}$ ) ranges from 0.98 to 6.86 mg/g

(mean 3.44 mg/g).

Theoretically, both multistage and conventional Rock-eval analyses are designed to quantify the entirety of residual oil and organic matter capable of hydrocarbon generation within shales. Thus, the sum of multistage Rock-Eval ( $S_{1-1}+S_{1-2}+S_{2-1}+S_{2-2}$ ) is expected to correspond closely with that of conventional Rock-Eval, i.e.,  $S_1+S_2$ . As exhibited in Fig. 4(a), the sum of multistage Rock-Eval is consistent well with that of conventional Rock-Eval, characterized by a regression slope nearing unity and a robust correlation coefficient of 0.9936. However, a notable discrepancy emerges when comparing the total oil contents calculated via multistage and conventional Rock-Eval (Table 3). Specifically,  $S_{T1}$  is always greater than  $S_{T2}$ , as demonstrated in Fig. 4(b). This divergence can be attributed to the extraction process, wherein free oil and oil adsorbed on pore surfaces are efficiently extracted, whereas oil dissolved in kerogen, often termed kerogen swelling oil or

**Table 3**  
Multistage Rock-Eval parameters of the studied shales.

Sample	Multistage Rock-Eval, mg/g						Conventional Rock-Eval, mg/g
	S <sub>1-1</sub>	S <sub>1-2</sub>	S <sub>2-1</sub>	S <sub>2-2</sub>	Free oil-S <sub>F</sub>	Total oil-S <sub>T1</sub>	Total oil-S <sub>T2</sub>
TY1	0.14	2.81	2.07	0.47	2.95	5.02	4.14
TY2	0.04	1.71	1.53	0.12	1.75	3.28	2.69
TY3	0.09	2.12	1.43	0.16	2.21	3.64	1.87
TY4	0.13	2.36	1.97	0.33	2.49	4.46	3.32
TY5	0.14	3.17	2.37	0.62	3.31	5.68	5.19
TY6	0.11	1.80	1.03	0.18	1.91	2.94	2.44
TY7	0.07	1.57	1.37	0.37	1.64	3.01	2.71
TY8	0.08	1.66	1.41	0.27	1.74	3.15	1.26
TY9	0.04	0.80	0.79	0.24	0.84	1.63	0.98
TY10	0.23	3.39	5.64	11.14	3.62	9.26	6.28
TY11	0.24	3.13	4.10	8.21	3.37	7.47	6.86
TY12	0.21	3.43	5.03	10.37	3.64	8.67	5.74
TY13	0.19	3.02	4.76	9.19	3.21	7.97	6.29
TY14	0.25	2.79	3.50	6.25	3.04	6.54	5.01
TY15	0.08	1.93	1.64	1.14	2.01	3.65	3.52
TY16	0.08	1.51	1.83	0.88	1.59	3.42	2.75
TY17	0.08	1.27	1.96	2.67	1.35	3.31	2.54
TY18	0.05	1.15	1.45	1.22	1.20	2.65	2.46
TY19	0.05	1.41	2.73	3.61	1.46	4.19	3.94
TY20	0.07	1.21	2.13	1.64	1.28	3.41	2.70
TY21	0.17	1.34	2.99	5.51	1.51	4.50	3.05
TY22	0.09	1.43	1.90	1.42	1.52	3.42	2.48
TY23	0.05	1.17	1.77	1.18	1.22	2.99	2.54
TY24	0.07	1.26	1.51	1.10	1.33	2.84	1.76

absorbed oil (Li et al., 2022b), is not entirely removable. Thus, S<sub>2</sub>\* typically encompasses a minor fraction of hydrocarbons that remain soluble in kerogen, culminating in a diminished S<sub>T2</sub> value. This assertion is corroborated by the relationship between S<sub>2-2</sub> and the differential between S<sub>T1</sub> and S<sub>T2</sub>, as exhibited in Fig. 4(c). The disparity between S<sub>T1</sub> and S<sub>T2</sub> is indicative of kerogen swelling oil, which should exhibit a strong correlation with the kerogen content as denoted by S<sub>2-2</sub>. Multistage Rock-Eval not only provides a more accurate evaluation of shale oil content but also can detect free and adsorbed oil. Moreover, it can also be found that both adsorbed and free oils exhibit a significant correlation with the total oil (Fig. 4(d)), aligning with findings from previous studies (Li et al., 2018a; Zhang et al., 2022a). Essentially, the sweet spots for shale oil resources are concomitantly the sweet spots for free oil.

### 3.2.2. Micro-occurrence of shale oil

High-resolution SEM images offer a vivid and precise visualization of the micro-occurrence characteristics of shale oil. In this study, SEM analyses were employed to delineate the micro-distribution of shale oil within unextracted samples. According to the principle of SEM backscatter imaging, the various components of shale can be distinguished based on their respective gray values. Specifically, the pyrite particles are discernible by the largest gray values and bright white appearance, whereas residual oil within shale pores and fractures is identified by its notably low gray values, appearing as dark black, followed by pores and fractures without oil, clay minerals, quartz/feldspar, and calcite/dolomite (Zhang et al., 2023c). Consequently, the SEM images of the unextracted state provide an efficacious approach to exploring the micro-occurrence of shale oil.

The SEM images of unextracted shales with high TOC and oil contents in different lithologies are shown in Fig. 5. High contents of felsic minerals result in the development of interparticle pores in felsic-rich shales (Fig. 5(a)). The interparticle pores are predominantly associated with brittle minerals such as quartz, feldspar, and calcareous constituents, manifesting as oil-saturated voids situated between or along the edges of brittle granules. Moreover, the intraparticle pores can also be identified in clay mineral aggregates,

alongside observable fractures. With a reduction in felsic mineral content, felsic shales exhibit an increased presence of clay minerals, leading to scenarios where quartz or feldspar granules are encased by clay minerals (Fig. 5(b)). As a result, felsic shales are characterized by the development of interparticle pores at granule edges and intraparticle pores within clay minerals. Predominantly, shale oil is found residing in fractures and large pores.

Calcareous-rich shales are characterized by an abundance of calcareous granules, as evidenced in Fig. 5(c). This composition gives rise to a multitude of interparticle pores nestled between calcareous granules. Moreover, the interparticle pores related to quartz or feldspar are also identified and typically saturated with oil. Thus, shale oil mainly occurs in the interparticle pores related to the calcareous or felsic minerals, particularly within the large pores. As the proportion of calcareous minerals diminishes and that of clay minerals escalates, an increased number of intraparticle pores emerge within calcareous shales (Fig. 5(d)). However, the primary occurrence of shale oil is within the larger interparticle pores. As exhibited in Fig. 5(e), a profusion of intraparticle pores is present within clay mineral aggregates, and a few interparticle pores are found at the granule edges. Furthermore, fractures are more pronounced. Oil predominantly saturates fractures, interparticle pores, and substantial intraparticle pores. It can thus be inferred that shale oil chiefly occurs within fractures, succeeded by interparticle pores associated with brittle granules, and extensive intraparticle pores within clay mineral aggregates. Both fractures and interparticle pores are conducive to shale oil, especially free oil.

Two-dimensional NMR T<sub>1</sub>–T<sub>2</sub> is an alternative technique for elucidating the shale oil micro-occurrence characteristics. Drawing from the prior research (Zhang et al., 2024a, 2024b), the T<sub>1</sub>–T<sub>2</sub> pattern was provided for shale oil reservoirs simultaneously containing oil and water, encompassing eight distinct regions based on the T<sub>2</sub> and T<sub>1</sub>/T<sub>2</sub> values, marked A to H as depicted in Fig. 6. Regions A to E refer to pore fluids, mainly relating to capillary-bound water, adsorbed oil, bound oil, movable oil, and movable water, respectively. However, regions F to H denote (pseudo-)solid protons, mainly linked to clay-bound water, asphaltene, and kerogen. Clay-bound water encompasses the protons related to clay minerals,

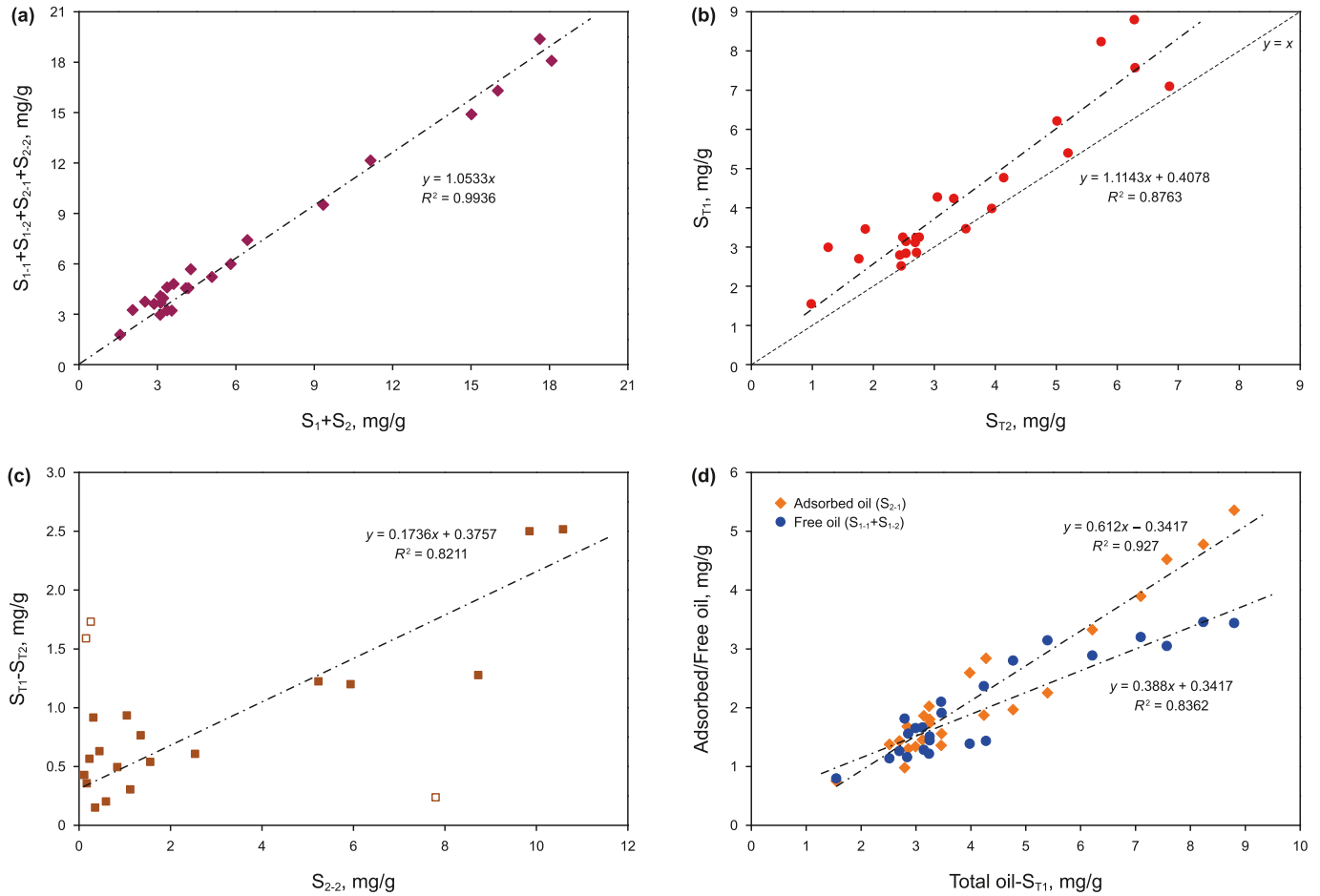


Fig. 4. Comparisons between multistage and conventional Rock-Eval in evaluating shale oil contents.

including structural and adsorbed water. The  $T_1$ – $T_2$  spectrum, predicated on this pattern, facilitates a comprehensive analysis of pore oil and water within shales.

The  $T_1$ – $T_2$  spectra of shale from diverse lithofacies indicate that argillaceous-rich (TY2) and argillaceous (TY3) shales exhibit the most pronounced amplitudes in region A, indicative of a substantial content of capillary-bound water within shales rich in clay minerals, as illustrated in Fig. 6. Furthermore, regions C are exceptionally significant in felsic (TY11), calcareous-rich (TY17 and TY21), and calcareous (TY19) shales, implying that a significant presence of bound oil within these lithologies. The presence of adsorbed oil is discernible in the  $T_1$ – $T_2$  spectra, characterized by lower amplitudes in region B. Additionally, region D, related to movable oil, is scarcely identifiable due to the near-complete dissipation of movable oil, aligning with the minimal  $S_{1-1}$  values obtained from multistage Rock-Eval (Table 3). Moreover, it is also observed that calcareous-rich and calcareous shales are generally more favorable for the enrichment of free oil, followed by felsic and felsic-rich shales, whereas argillaceous-rich and argillaceous shales are distinguished by elevated contents of pore water.

To corroborate the precision of NMR  $T_1$ – $T_2$  analysis in determining the micro-distributions of pore fluids, the amplitudes of regions A to E, corresponding to pore oil and water, were quantitatively derived and juxtaposed with clay mineral content and multistage Rock-Eval data, as depicted in Fig. 7. Capillary-bound water correlates positively with clay minerals (Fig. 7(a)). The higher the clay mineral content leads to reduced compaction resistance in shale and smaller pore-throats, resulting in

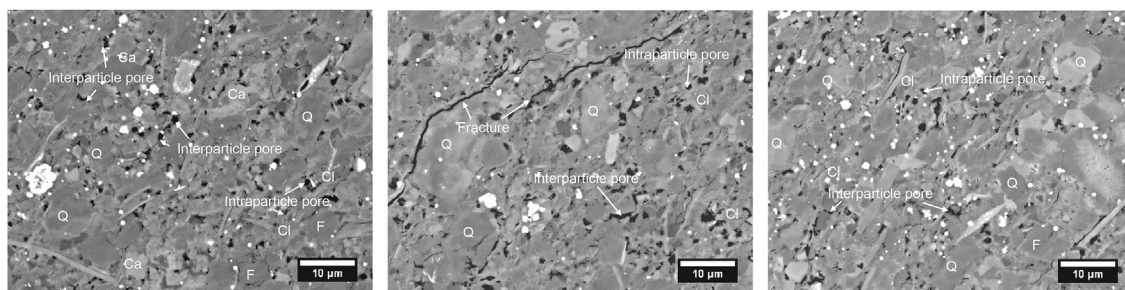
heightened capillary-bound water content. Total oil, adsorbed, and free oil contents detected by NMR  $T_1$ – $T_2$  spectra correlate well with those from multistage Rock-Eval (Fig. 7(b), (c), and (d)), affirming the capability of the NMR  $T_1$ – $T_2$  spectrum to analyze the shale oil occurrence accurately.

Previous studies have established that  $T_2$  values indicate pore sizes, with larger  $T_2$  values denoting larger pores (Li et al., 2015b, 2023). Specifically, within shale oil reservoirs,  $T_2$  values under 1 ms are primarily associated with pores smaller than 100 nm (micro- and minipores),  $T_2$  values between 1 and 20 ms correlate with pores ranging from 100 to 1000 nm (mesopores), and  $T_2$  values exceeding 20 ms are linked to pores larger than 1000 nm (macropores) (Zhang et al., 2018). As a result, capillary-bound water and adsorbed oil predominantly occupy pores smaller than 100 nm, mesopores are largely filled with bound oil, and macropores are the main domain of movable oil (Zhang et al., 2022a, 2023b), although movable oil is largely lost. Hence, pore water significantly impacts the occurrence of adsorbed oil, followed by bound oil, and exerts minimal influence on movable oil.

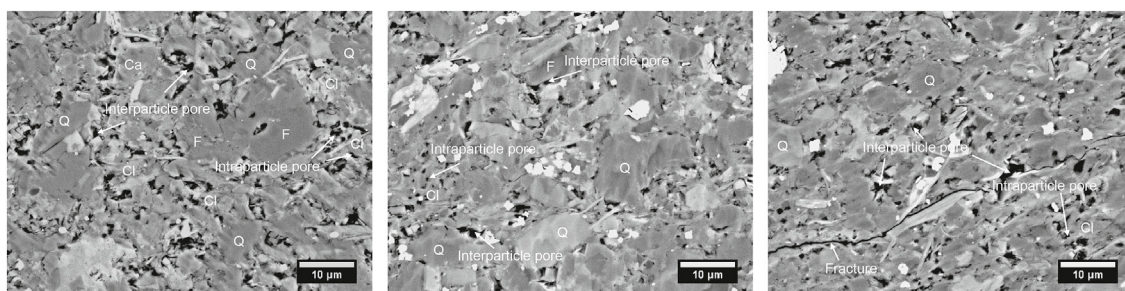
### 3.3. LTNA/D of the unextracted and extracted shales

#### 3.3.1. Nitrogen adsorption and desorption isotherms

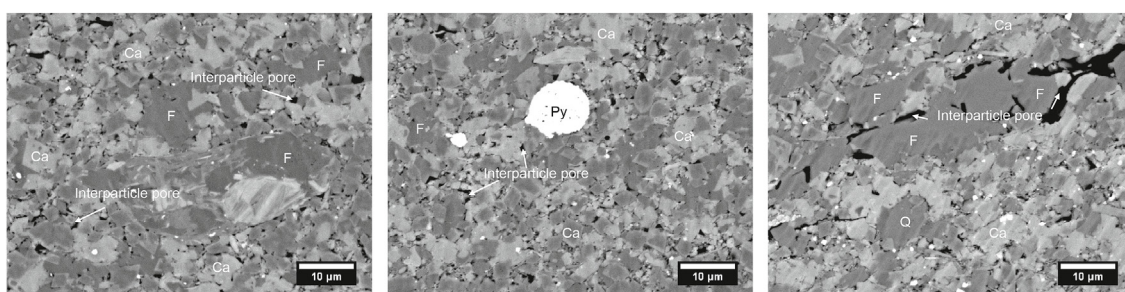
Typical nitrogen adsorption and desorption isotherms of the selected shales are exhibited in Figs. 8 and 9. The selected shales can be classified into two groups based on the characteristics of nitrogen isotherms at unextracted and extracted states. Type A adsorption isotherms belong to Type II isotherms according to



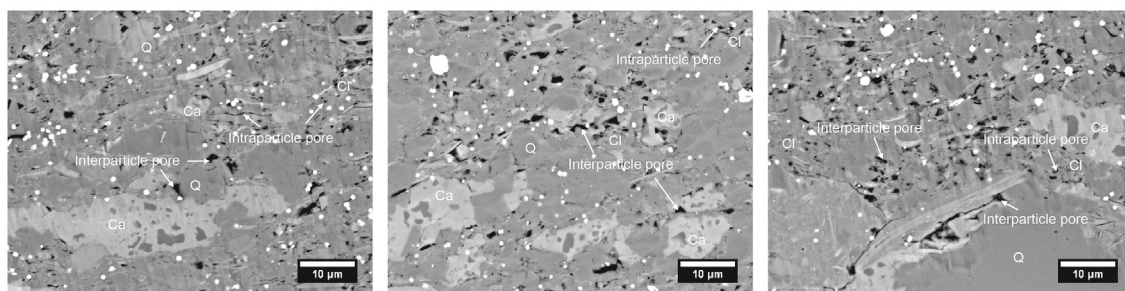
(a) TY22 (Type B), felsic-rich shale, TOC = 1.20%,  $S_{T1}$  = 3.25 mg/g



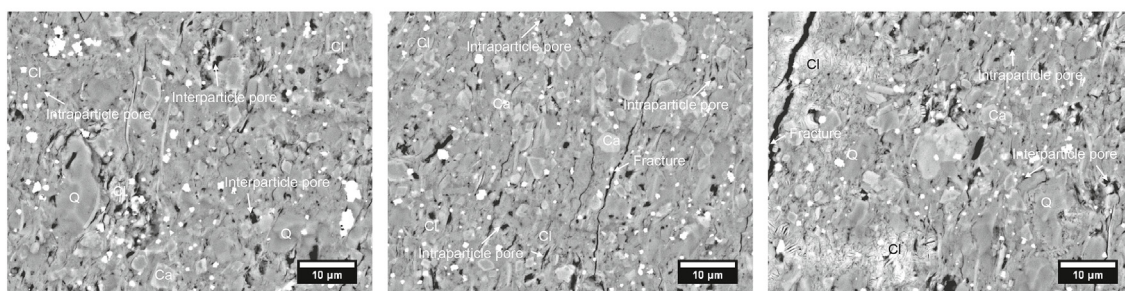
(b) TY23 (Type B), felsic shale, TOC = 0.94%,  $S_{T1}$  = 2.84 mg/g



(c) TY21 (Type A), calcareous-rich shale, TOC = 2.20%,  $S_{T1}$  = 4.28 mg/g



(d) TY19 (Type A), calcareous shale, TOC = 1.53%,  $S_{T1}$  = 3.98 mg/g



(e) TY4 (Type B), argillaceous shale, TOC = 1.55%,  $S_{T1}$  = 4.24 mg/g

**Fig. 5.** SEM images of selected shales in different lithofacies. Q, F, Ca, Cl, and Py refer to quartz, feldspar, calcareous minerals, clay minerals, and pyrite, respectively.

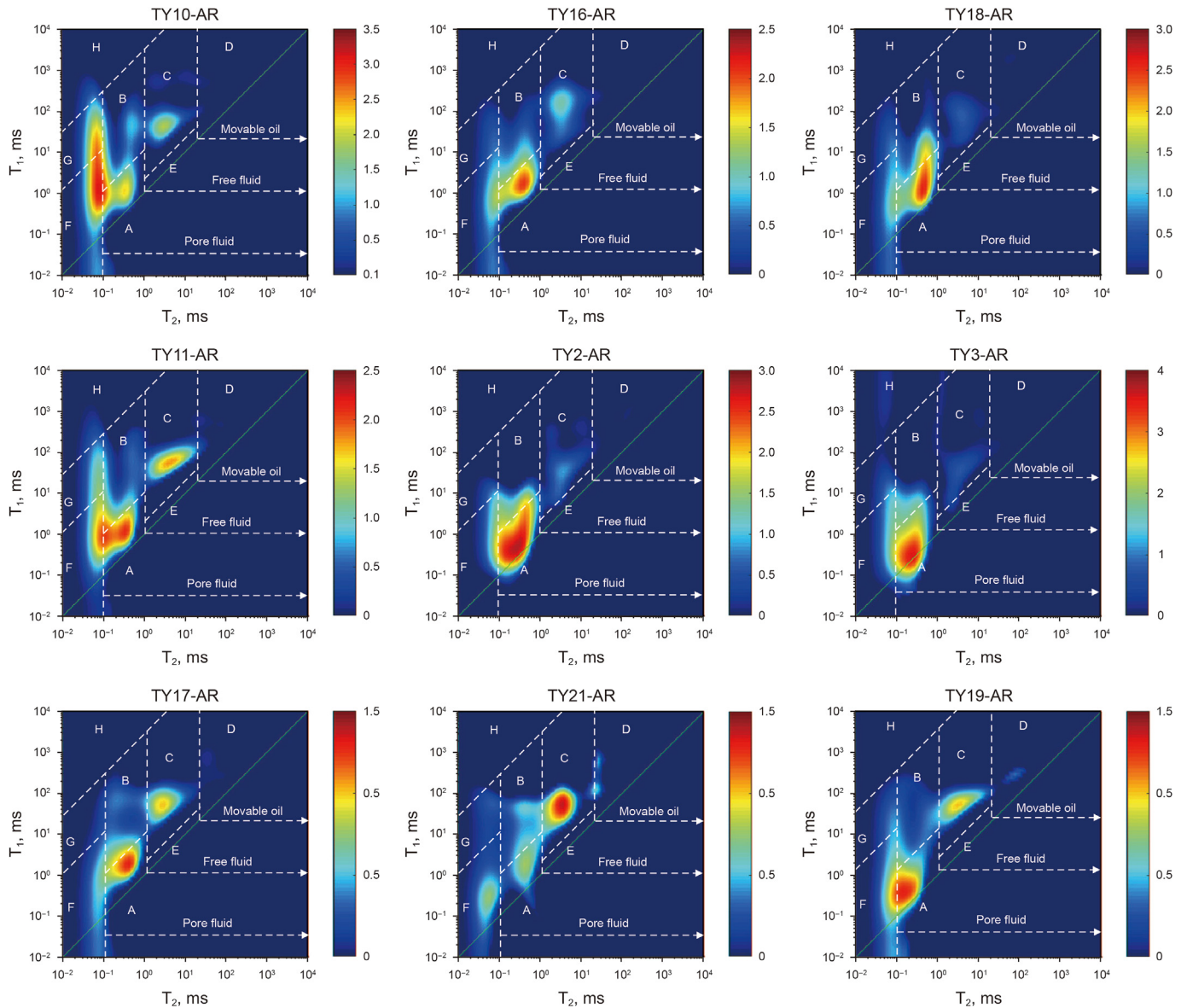


**Fig. 6.**  $T_1$ – $T_2$  spectra of the studied shales at AR (unextracted) state. A and E refer to capillary-bound and movable water, respectively; B, C, and D are the adsorbed, bound, and movable oils, respectively; F, G, and H represent the clay-bound water, asphaltene, and kerogen, respectively. TY10, TY16, and TY18 are felsic-rich shales; TY11 is felsic shale; TY2 and TY3 are argillaceous-rich and argillaceous shales, respectively; TY17 and TY21 are calcareous-rich shales, and TY19 is the calcareous shale.

IUPAC (International Union of Pure and Applied Chemistry) (Fig. 8). As the relative pressure ( $P/P_0$ ) nears 1, there is a marked escalation in the nitrogen adsorption capacity. The isotherms of unextracted Type A shales are distinguished by minimal hysteresis loops, aligning with Type H3 hysteresis loops, which suggests that the predominant pores in these shales are of the parallel-plate variety. Post-extraction, however, the hysteresis loops undergo significant alteration, exhibiting a hybrid Type H2–H3 loop pattern, indicative of the development of both parallel-plate and ink-bottle pores. This observation leads to the inference that residual shale oil is primarily situated within ink-bottle pores, mainly related to the interparticle pores (Fig. 5(c) and (d)). Moreover, a notable increase in nitrogen adsorption capacity is observed following extraction.

Type B nitrogen adsorption isotherms are similar to Type A, relating to Type II isotherms (Fig. 9). Nevertheless, the hysteresis loops for Type B shales remain consistent before and after extraction, corresponding to a mixed Type H2–H3 hysteresis loop, which

denotes the presence of parallel-plate and ink-bottle pores within Type B shales. This suggests that shale oil occurs in parallel-plate and ink-bottle pores, predominantly corresponding to the intra-particle pores in clay minerals and interparticle pores associated with brittle granules, respectively (Fig. 5(a), (b), and (e)). When compared to Type A shales, the increments in nitrogen adsorption at equivalent relative pressures post-extraction are less pronounced for Type B shales (Figs. 8 and 9). Conversely, irrespective of the extraction status, Type A shales exhibit lower nitrogen adsorption capacities than Type B shales at the same relative pressures, suggesting that Type A shales possess larger pore volumes.

The mineral compositions and shale oil contents of Types A and B shales are displayed in Fig. 10. Type A shales are characterized by higher concentrations of felsic and calcareous minerals but lower clay mineral content, whereas Type B shales contain greater quantities of clay minerals, succeeded by felsic minerals, and lesser

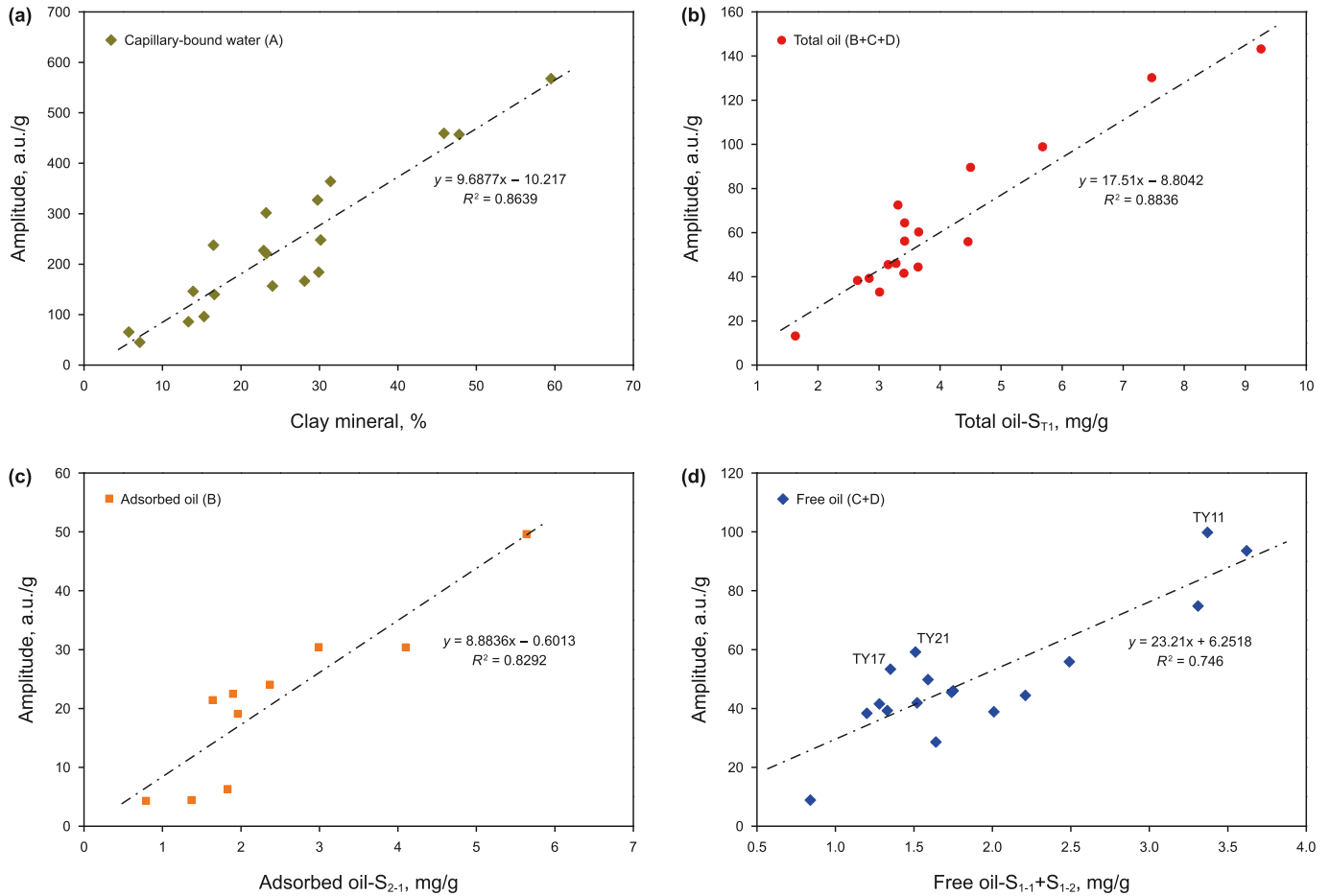


Fig. 7. Relationships between NMR  $T_1$ – $T_2$  amplitudes with clay minerals (a) and shale oil contents ((b)–(d)).

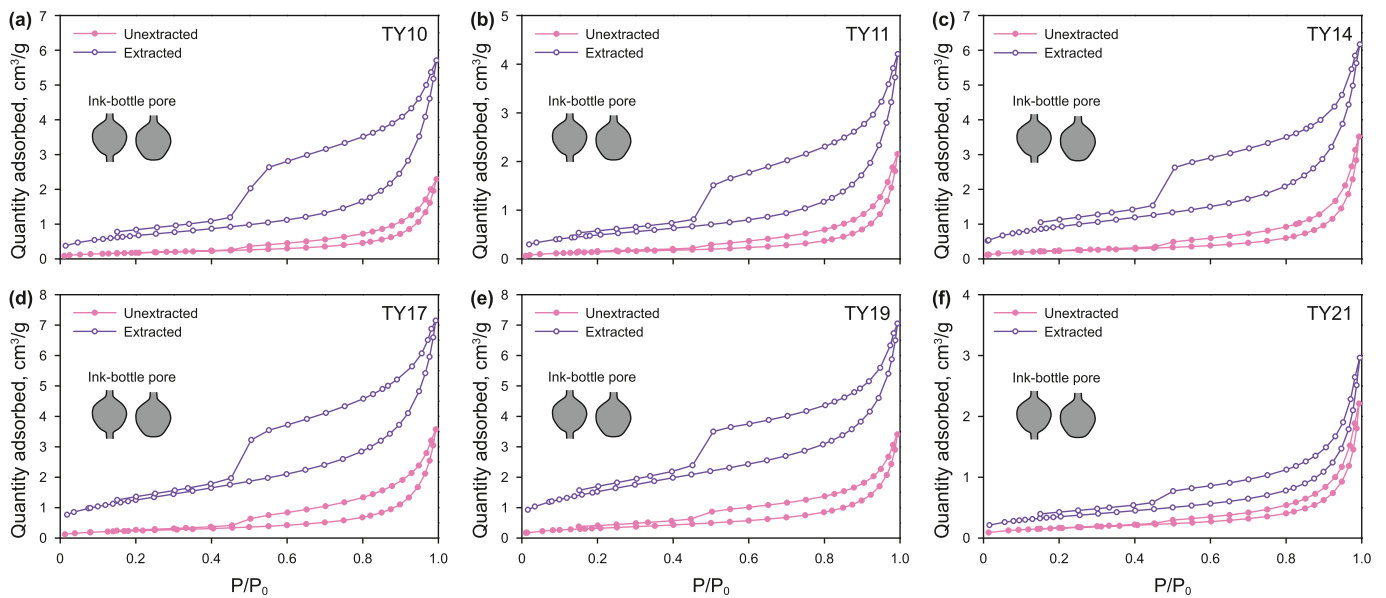


Fig. 8. Nitrogen adsorption-desorption isotherms of unextracted and extracted shales for Type A.

amounts of calcareous minerals (Fig. 10(a)). The TOC contents of Type A shales are larger, predominantly aligning with organic-rich shales exhibiting TOC values exceeding 1.5% (Fig. 10(b)). The

adsorbed, free, and total oil contents of Type A shales are all larger than those of Type B shales. This indicates that shales with elevated levels of felsic or calcareous minerals, corresponding to felsic(-rich)

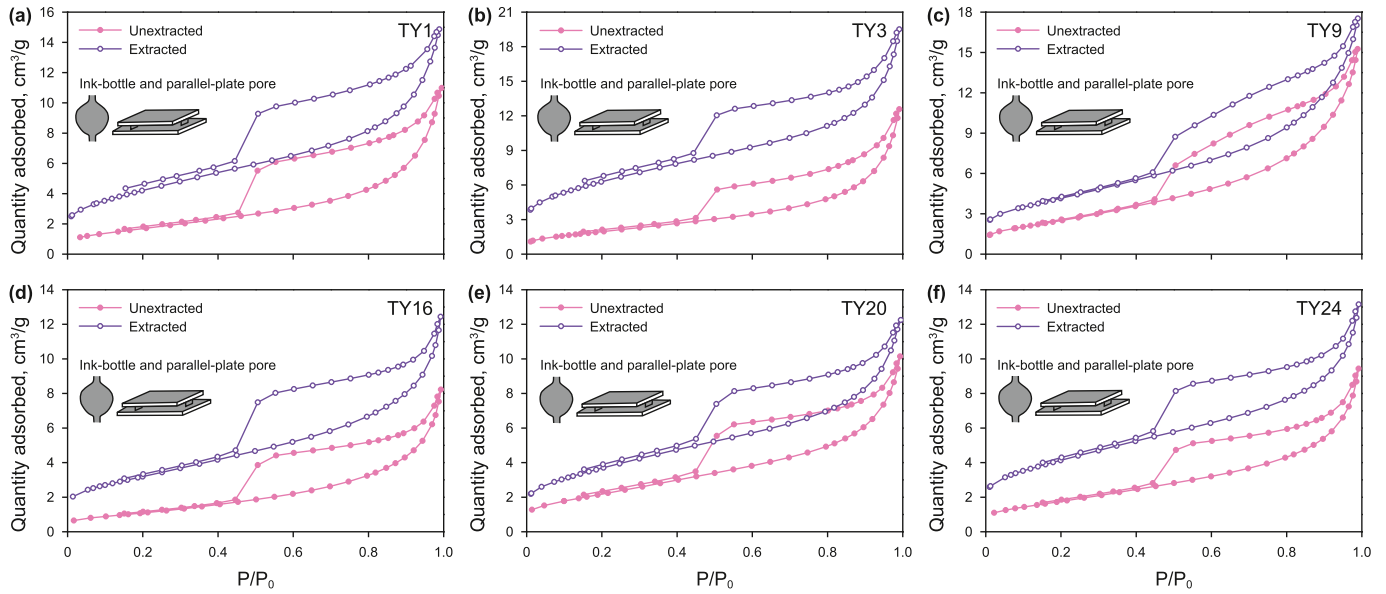


Fig. 9. Nitrogen adsorption-desorption isotherms of unextracted and extracted shales for Type B.

or calcareous(-rich) shales, generally harbor higher concentrations of shale oil, corroborating the NMR  $T_1$ – $T_2$  spectra in Fig. 6.

3.3.2. Micro-pore structures parameters

The pore structure parameters from LTNA/D of the unextracted and extracted shales are detailed in Tables 4 and 5. BET SSA before extraction is between 0.51 and 9.52  $m^2/g$ , with a mean of 4.22  $m^2/g$ , while after extraction, BET SSA increases with an average of 10.21  $m^2/g$ , varying from 1.27 to 22.53  $m^2/g$ . The total pore volume (TPV) of unextracted shale spans from 3.33 to 23.60  $\times 10^{-3} cm^3/g$  (mean 12.16  $\times 10^{-3} cm^3/g$ ). Correspondingly, the TPV of extracted shale averages 18.58  $\times 10^{-3} cm^3/g$ , ranging from 4.73 to 30.31  $\times 10^{-3} cm^3/g$ . The average pore diameter (da) at the unextracted state varies from 7.63 to 26.73 nm (mean 15.28 nm), and it at the extracted state presents a mean of 8.72 nm (5.36–15.24 nm). Compared with the unextracted state, BET SSA and TPV increase, while the da decreases, as shown in Fig. 11, suggests an enhanced detection of smaller pores after extraction. Moreover, BET SSA before and after extraction shows a good positive correlation, so do TPV and da. BET SSA shows excellent positive correlations with TPV of both unextracted and extracted shales (Fig. 12(a)), while good

negative correlations are observed between da and BET SSA, as exhibited in Fig. 12(b). Furthermore, Type B shales generally exhibit larger TPV and BET SSA but smaller da compared to Type A shales (Figs. 11 and 12).

To further analyze the changes in pore structures before and after extraction, the PV and SSA of pores in different scales were quantified and compared (Tables 4 and 5, Fig. 13). This study adopted the pore classification scheme provided by authors, i.e., micropore (<25 nm), minipore (25–100 nm), mesopore (100–1000 nm), and macropore (>1000 nm) (Zhang et al., 2017). The TPV of the unextracted shale mainly originates from minipores, followed by micropores and mesopores. The PV of minipores ranges from 1.82 to 21.20  $\times 10^{-3} cm^3/g$  (average 6.36  $\times 10^{-3} cm^3/g$ ), and the PV of micropores averages 5.10  $\times 10^{-3} cm^3/g$  (0.03–13.37  $\times 10^{-3} cm^3/g$ ). The PV of mesopores is characterized by a low average value of 1.63  $\times 10^{-3} cm^3/g$ , ranging from 0.56 to 4.71  $\times 10^{-3} cm^3/g$ . After extraction, the TPV increases and primarily originates from micropores, averaging PV of 12.57  $\times 10^{-3} cm^3/g$  (2.00–21.46  $\times 10^{-3} cm^3/g$ ), while the PV values of both minipores and mesopores slightly decrease, averaging at 4.96  $\times 10^{-3}$  and 1.04  $\times 10^{-3} cm^3/g$ , respectively. This trend aligns with previous

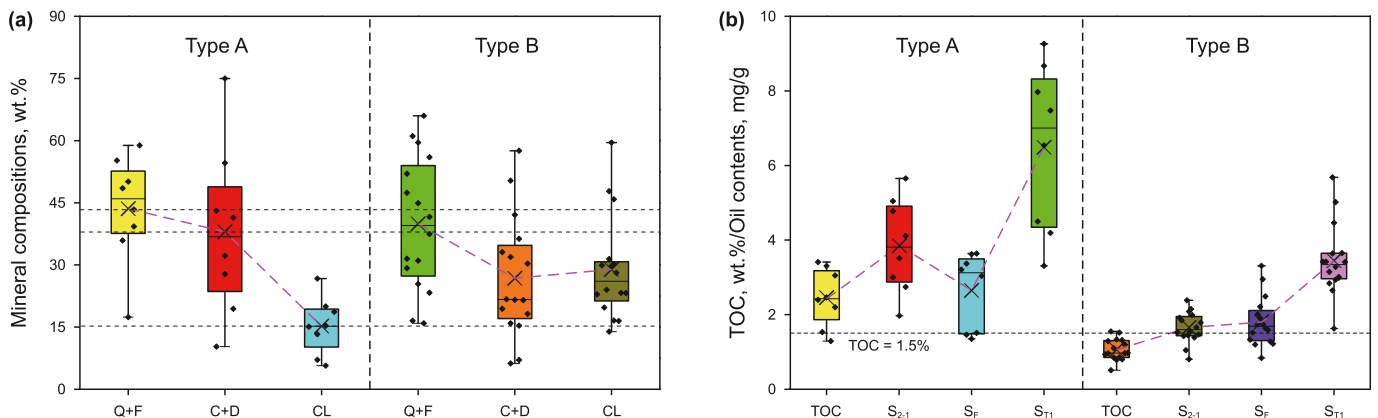


Fig. 10. Comparisons between Types A and B shales in mineral compositions (a) TOC, and shale oil contents (b) Q, F, C, D, and CL denote the quartz, feldspar, calcite, dolomite, and clay minerals;  $S_F$  is free oil, and  $S_{T1}$  is the total oil obtained from multistage Rock-Eval.

**Table 4**  
Pore structure parameters from LTNA/D of the unextracted shales.

Sample	Type A or B	BET SSA, m <sup>2</sup> /g	TPV, 10 <sup>-3</sup> cm <sup>3</sup> /g	Da, nm	PV, 10 <sup>-3</sup> cm <sup>3</sup> /g			SSA, m <sup>2</sup> /g		
					Micro-	Mini-	Meso-	Micro-	Mini-	Meso-
TY1	B	6.34	17.00	10.72	10.59	6.89	0.86	7.71	0.55	0.02
TY2	B	8.65	20.71	9.57	13.37	7.92	1.05	10.31	0.64	0.03
TY3	B	7.29	19.46	10.68	11.53	8.01	1.28	8.46	0.64	0.03
TY4	B	6.03	18.87	12.51	7.68	7.95	4.71	6.73	1.24	0.19
TY5	B	2.94	12.32	16.77	6.78	5.61	0.77	3.73	0.44	0.02
TY6	B	5.43	17.62	12.98	0.03	15.34	3.78	0.06	7.60	0.17
TY7	B	4.84	15.23	12.58	0.11	12.70	3.78	0.21	6.51	0.17
TY8	B	4.67	14.96	12.80	0.10	12.41	3.74	0.20	6.23	0.17
TY9	B	9.52	23.60	9.91	0.30	21.20	4.42	0.64	12.16	0.20
TY10	A	0.63	3.55	22.44	1.23	1.89	0.56	0.64	0.14	0.01
TY11	A	0.51	3.33	26.08	1.00	1.85	0.57	0.47	0.14	0.01
TY12	A	0.85	4.61	21.71	1.62	2.36	0.79	0.84	0.18	0.02
TY13	A	1.30	6.86	20.31	2.36	3.79	0.93	1.26	0.29	0.02
TY14	A	0.81	5.44	26.73	1.57	2.89	1.12	0.71	0.22	0.03
TY15	B	1.96	8.48	17.33	4.26	3.65	1.11	2.45	0.29	0.03
TY16	B	4.18	12.72	12.18	7.81	4.89	1.15	5.44	0.39	0.03
TY17	A	0.88	5.53	25.20	1.90	2.96	0.87	0.88	0.23	0.02
TY18	B	5.33	14.22	10.66	8.41	5.62	1.34	6.50	0.47	0.03
TY19	A	1.18	5.27	17.92	2.11	2.55	0.84	1.24	0.20	0.02
TY20	B	8.23	15.69	7.63	10.78	5.08	1.18	9.59	0.43	0.03
TY21	A	0.59	3.42	23.26	1.03	1.82	0.67	0.54	0.13	0.02
TY22	B	5.76	13.09	9.09	8.32	4.66	1.24	6.93	0.38	0.03
TY23	B	6.79	15.21	8.96	9.79	5.47	1.23	8.12	0.46	0.03
TY24	B	6.64	14.59	8.80	9.62	5.00	1.24	7.98	0.42	0.03

TPV is the total pore volume; PV denotes the pore volume; da refers to the average pore diameter; SSA represents the specific surface area; micro-, mini-, and meso- are the micropores, minipores, and mesopores, respectively.

**Table 5**  
Pore structure parameters from LTNA/D of the extracted shales.

Sample	Type A or B	BET SSA, m <sup>2</sup> /g	TPV, 10 <sup>-3</sup> cm <sup>3</sup> /g	Da, nm	PV, 10 <sup>-3</sup> cm <sup>3</sup> /g			SSA, m <sup>2</sup> /g		
					Micro-	Mini-	Meso-	Micro-	Mini-	Meso-
TY1	B	15.10	23.81	6.09	17.13	6.04	0.64	15.12	0.49	0.02
TY2	B	17.60	27.04	5.98	19.31	6.74	1.00	17.43	0.50	0.03
TY3	B	22.53	30.31	5.36	21.42	7.18	1.70	20.47	0.56	0.04
TY4	B	16.09	29.98	6.99	21.15	7.49	1.34	17.84	0.60	0.04
TY5	B	8.56	17.88	8.04	11.99	5.12	0.77	8.78	0.39	0.02
TY6	B	13.54	25.71	7.17	18.78	6.05	0.87	14.81	0.46	0.02
TY7	B	11.87	22.74	7.17	15.89	5.98	0.87	13.29	0.46	0.02
TY8	B	5.97	14.75	9.15	9.42	4.32	1.01	7.11	0.33	0.03
TY9	B	15.05	28.76	7.20	21.46	6.47	0.83	16.64	0.49	0.02
TY10	A	2.45	9.24	15.10	4.89	3.48	0.87	2.64	0.27	0.02
TY11	A	1.77	6.76	15.24	3.25	2.72	0.79	1.81	0.20	0.02
TY12	A	3.51	13.05	14.88	7.11	4.81	1.13	3.91	0.36	0.02
TY13	A	5.98	18.28	12.23	10.20	6.90	1.18	6.26	0.50	0.03
TY14	A	3.37	9.93	11.78	5.44	3.59	0.89	3.47	0.27	0.02
TY15	B	9.92	16.25	6.55	11.03	4.04	1.19	10.01	0.30	0.03
TY16	B	11.48	20.16	7.02	13.87	5.00	1.28	12.11	0.37	0.03
TY17	A	4.56	11.64	10.22	7.04	3.69	0.91	4.95	0.28	0.02
TY18	B	13.63	21.78	6.39	15.47	5.10	1.21	13.91	0.39	0.03
TY19	A	5.53	11.39	8.23	6.82	3.66	0.90	5.72	0.27	0.02
TY20	B	13.31	19.86	5.97	14.49	4.48	0.90	13.78	0.34	0.02
TY21	A	1.27	4.73	14.88	2.00	1.98	0.74	1.24	0.14	0.02
TY22	B	13.55	19.65	5.80	13.96	4.46	1.23	13.47	0.33	0.03
TY23	B	13.70	21.53	6.29	14.85	5.29	1.40	13.72	0.40	0.04
TY24	B	14.65	20.60	5.62	14.79	4.53	1.28	13.88	0.34	0.03

TPV is the total pore volume; PV denotes the pore volume; da refers to the average pore diameter; SSA represents the specific surface area; micro-, mini-, and meso- are the micropores, minipores, and mesopores, respectively.

research findings, where PVs of minipores and mesopores exhibit a marginal reduction in the PSD after extraction (Bai et al., 2022; Zhang et al., 2023a).

The SSA of micropores at unextracted state ranges from 0.06 to 10.31 m<sup>2</sup>/g (mean 3.82 m<sup>2</sup>/g), while the SSA of minipores is between 0.13 and 12.16 m<sup>2</sup>/g (mean 1.68 m<sup>2</sup>/g). The mesopores SSA has a low average value of 0.06 m<sup>2</sup>/g (0.01–0.20 m<sup>2</sup>/g). After extraction, the micropore SSA increases remarkably, averaging at

10.52 m<sup>2</sup>/g, ranging from 1.24 to 20.47 m<sup>2</sup>/g. A similar phenomenon can be observed in that the SSA values of both minipores and mesopores slightly decrease. The PV and SSA of micropores, minipores, and mesopores before and after extraction are exhibited in Fig. 13. Both PV and SSA of micropores, minipores, and mesopores in Type B shales are consistently larger than those in Type A shales. Compared with Type A shales, Type B shales demonstrate a more pronounced increase in the PV and SSA across all pore scales,

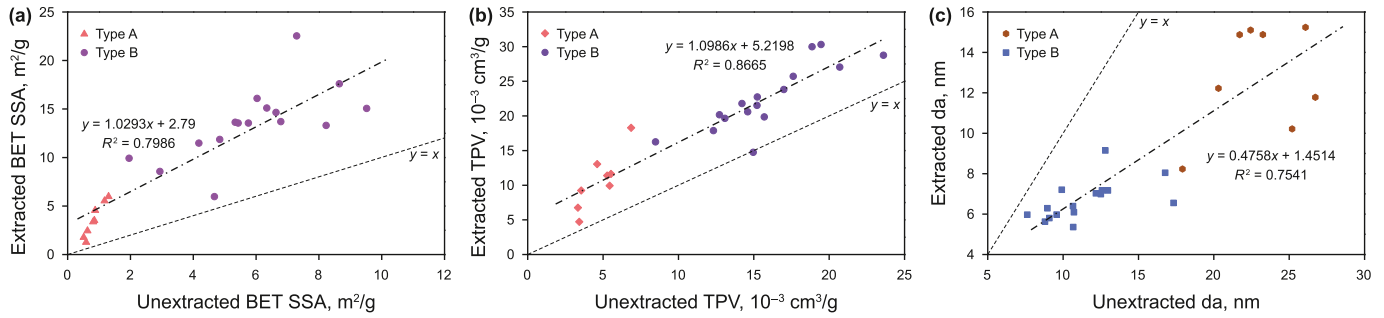


Fig. 11. BET SSA (a), total pore volume (TPV) (b), and average pore diameter (da) (c) before and after extraction.

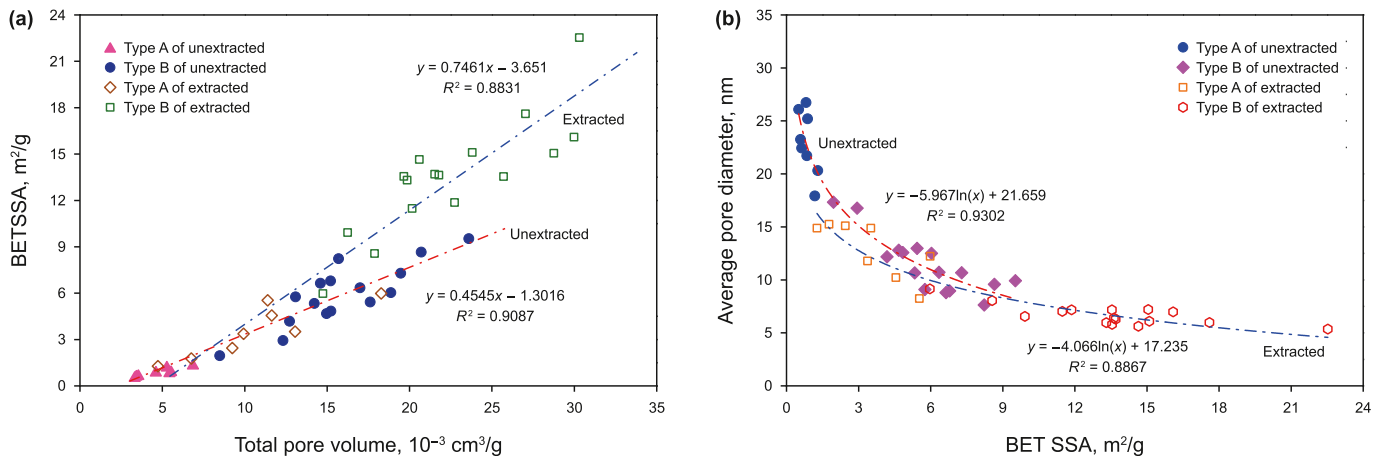


Fig. 12. Relationships between BET SSA with total pore volume (a) and average pore diameter (b).

suggesting a more extensive development of nano-scale pores. However, this phenomenon seems to contradict with the oil contents in Types A and B shales, as shown in Fig. 10(b). Specifically, Type A shales generally possess higher oil contents (total, adsorbed, and free oil) compared to Type B shales, whereas the PV and SSA metrics are inversely related (Fig. 13). This discrepancy may be attributed to the limitations of LTNA/D as a microscopic detection technique, which primarily identifies pores smaller than 200 nm, thereby overlooking larger mesopores and macropores. Nevertheless, NMR  $T_1$ – $T_2$  spectra show that most free oil (bound and movable oil) occurs in large mesopores macropores. The PV data derived from LTNA/D do not fully capture the distribution of all shale oil, particularly free oil. As a result, Type B shales exhibit larger PV and SSA but lower shale oil contents. In addition, it can be inferred that the large mesopores and macropores of Type A shales are more developed. Type A shales are more conducive to the enrichment and flow of shale oil.

### 3.3.3. Pore size distributions

There is a significant difference in the PSDs between Types A and B shales before extraction, as demonstrated in Fig. 14. The PSDs of Type A shales are unimodal and characterized by the dominant right peaks located at pore sizes of 40–200 nm. The PSDs of Type B shales are bimodal, with peaks at about 3 and 40 nm. After extraction, the PVs in PSDs of Type A shales increase from micropores to mesopores, as shown in Fig. 14(a)–(f), indicating the dispersion of shale oil across a spectrum of pore dimensions. The PSDs of Type A shales after extraction are unimodal or bimodal. However, for Type B shales, a notable increase in the amplitudes of the left peaks, corresponding to micropores, is observed, while the

right peaks, indicative of minipores and mesopores, either persist unchanged or marginally intensify (Fig. 14(g)–(l)). This pattern intimates that residual shale oil is predominantly sequestered within micropores, where it is adsorbed in Type B shales. The PSDs are mostly bimodal, with dominant left peaks at about 3 nm.

To elucidate the PSDs of residual shale oil, the differential PSDs before and after extraction were analyzed and are depicted in Fig. 15. The PSDs of residual oil in Type A shales are diverse and bimodal with the left peaks centered around 3 nm and right peaks in the vicinity of 20–40 nm (Fig. 15(a)). In contrast, the PSDs of residual oil in Type B shales are predominantly unimodal, with dominant left peaks under 3 nm (Fig. 15(b)), indicating that residual oil in Type B shales mainly occurs in micropores, especially small micropores less than 10 nm. The PSDs of residual shale oil also suggest that Type A shales are more favorable for shale oil accumulation than Type B shales.

### 3.3.4. Fractal characteristics

Fractal theory serves as a potent analytical approach for delineating the complexity and heterogeneity of pore structure. Based on the nitrogen adsorption isotherms, the fractal characteristics of shale micro-pore structures can be accurately described by the FHH (Frenkel-Halsey-Hill) model, which can be expressed as follows (Yao et al., 2008; Li et al., 2016).

$$\ln\left(\frac{V}{V_0}\right) = A\left(\ln\left(\ln\left(\frac{P_0}{P}\right)\right)\right) + C \quad (1)$$

where  $V$  refers to the adsorption volume at the pressure of  $P$ ;  $V_0$  denotes the volume of monolayer coverage;  $P_0$  is the nitrogen saturation vapor pressure at 77 K;  $C$  is a constant. If shale pore

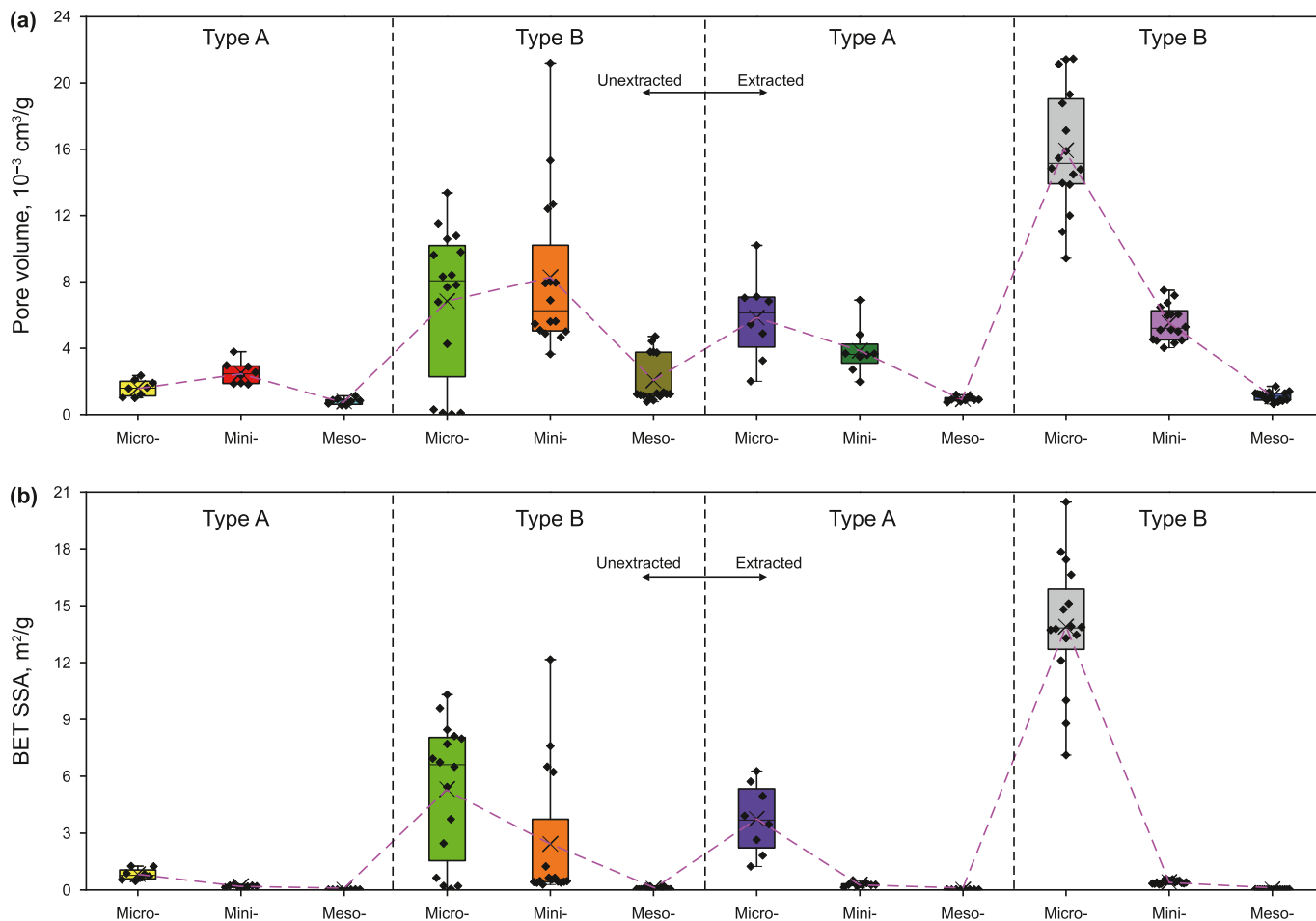


**Fig. 13.** Pore volume and SSA of micropores, minipores, and mesopores at unextracted and extracted states. Micro-, mini-, and meso- are the micropores, minipores, and mesopores, respectively.

structures are fractal,  $\ln(V)$  will linearly correlate with  $\ln(\ln(P_0/P))$ . Fractal dimension can be determined by the slope  $A$ .

$$D = A + 3 \tag{2}$$

The FHH plots of Types A and B shales before and after extraction are exhibited in Fig. 16, exemplified by samples TY10 and TY1, respectively. Two distinct segments were observed with the relative pressure ( $P/P_0$ ) of 0.5 as the threshold. Correspondingly, two fractal dimensions, i.e.,  $D_1$  and  $D_2$ , can be defined.  $D_1$  is determined with  $P/P_0$  less than 0.5, associated with the monolayer and multilayer adsorption, primarily reflecting the pore surface complexity (Yao et al., 2008). When the  $P/P_0$  is larger than 0.5, mainly corresponding to capillary condensation,  $D_2$  can be obtained to describe the complexity and heterogeneity of the pore structure.

The fractal dimensions of the selected shales before and after extraction are listed in Table 6. For the unextracted shales,  $D_1$  is between 2.3983 and 2.4891, averaging 2.4366.  $D_2$  varies from 2.4144 to 2.7395 (mean 2.5842), which is larger than  $D_1$ , implying that the pore structure is more complex than the pore surface. After extraction, the average value of  $D_1$  increases to 2.5207, ranging from 2.4500 to 2.5705, and  $D_2$  is between 2.5197 and 2.8140, with a mean of 2.7137. Both  $D_1$  and  $D_2$  at the extracted state are larger than those at the unextracted state, suggesting that pore fluids will diminish the heterogeneity and complexity of shale pore surfaces and pore structures. In other words, pore fluids preferentially adsorb on more complex pore surfaces (Wang et al., 2016). Nevertheless, for

the unextracted state,  $D_1$  of Type A shales is generally larger than that of Type B shales, with no apparent correlation between  $D_1$  and BET SSA (Fig. 17(a)), indicating potential coverage of pore surfaces by residual oil. However,  $D_1$  of Type A shales is mainly lower than that of Type B shales after extraction, with a clear positive correlation with BET SSA, meaning that the more complex the pore surface, the larger the SSA is. However,  $D_2$  of Type A shales is mainly lower than that of Type B shales regardless of before and after extraction (Fig. 17(b)). And there are excellent negative correlations between  $D_2$  and average pore diameter, suggesting that the development of larger pores is associated with a less complex pore structure. Overall, Type A shales tend to exhibit simpler pore surfaces and structures compared to Type B shales (see Fig. 18).

### 3.4. Controlling factors of shale oil occurrence

#### 3.4.1. Organic matter

Hydrocarbons within shales, encompassing both oil and gas, are fundamentally derived from organic matter in shales, thus the organic matter characteristics, such as types, maturity, and contents, are pivotal in dictating the occurrence and distribution of shale oil (Zhang et al., 2019; Hu et al., 2021). The organic matter content (TOC) is regarded as the key factor controlling the contents and occurrence states of shale oil (Wang et al., 2015; Zhang et al., 2019). Overall, the larger the content of organic matter, the more oil is generated during the mature stage, corresponding to a high

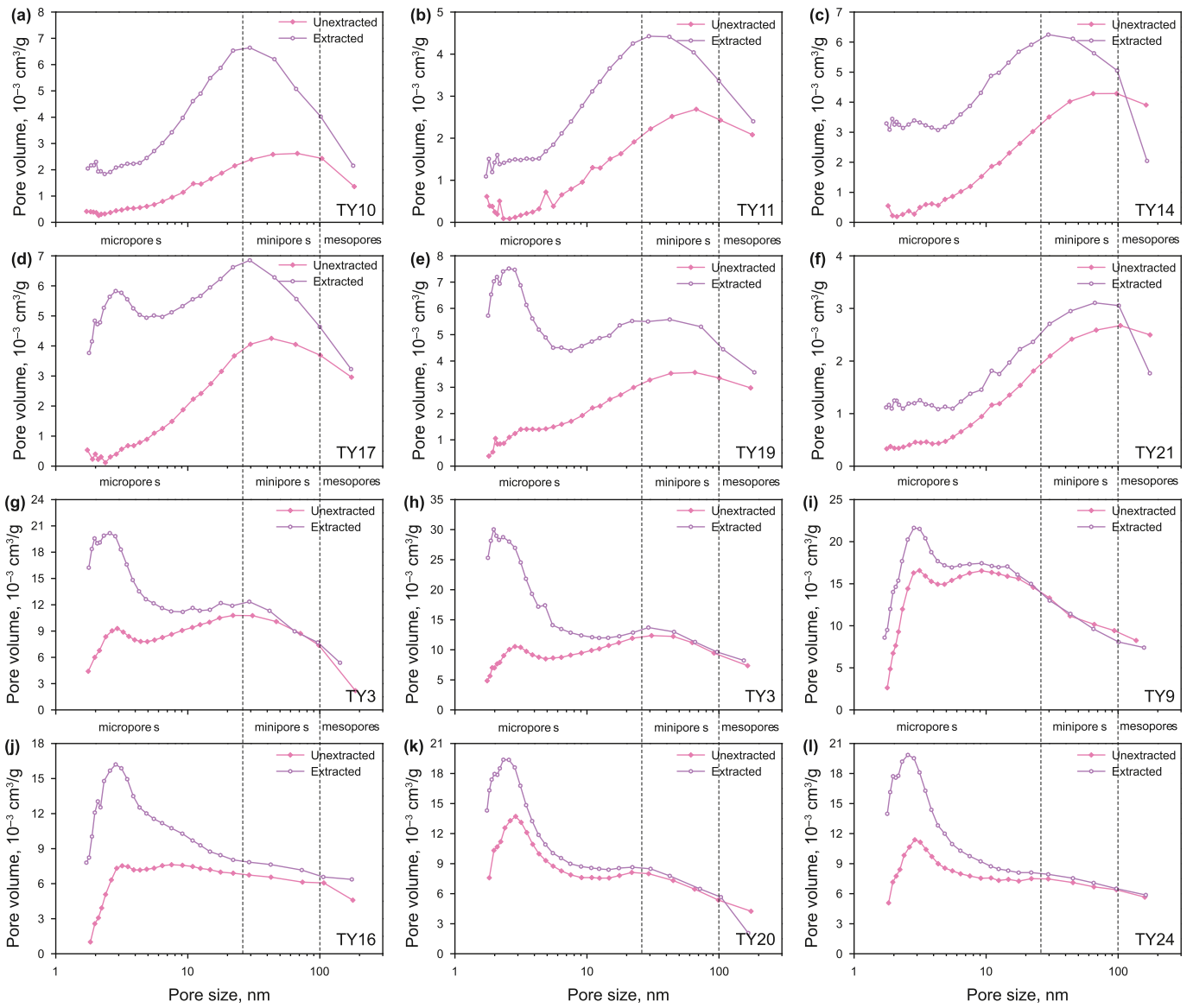


Fig. 14. Pore size distributions of shales at the unextracted and extracted states for Types A ((a)–(f)) and B ((g)–(l)).

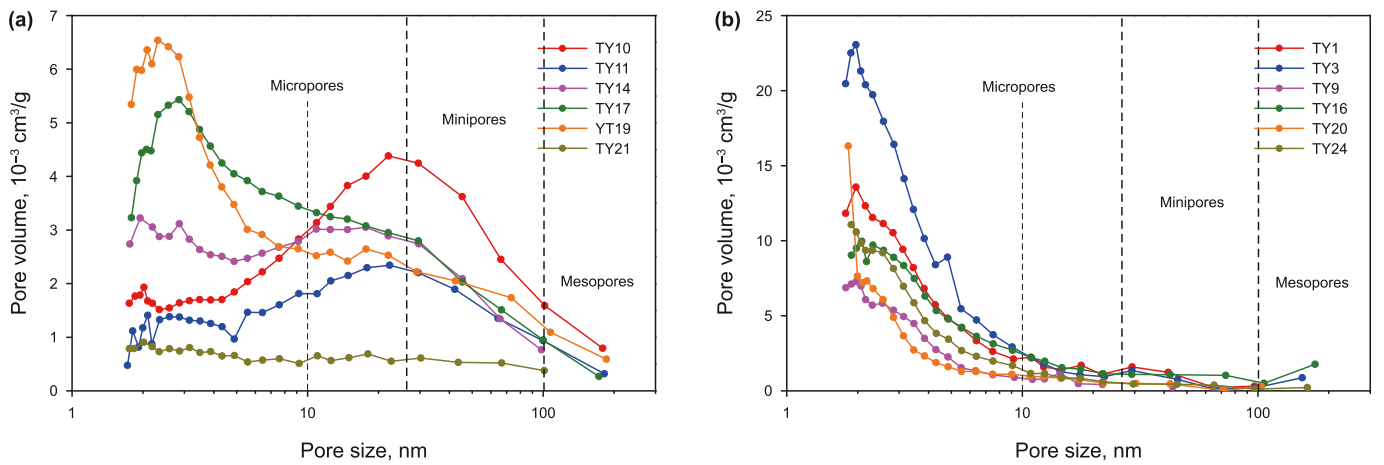


Fig. 15. Difference of pore size distribution between unextracted and extracted states for Types A (a) and B (b).

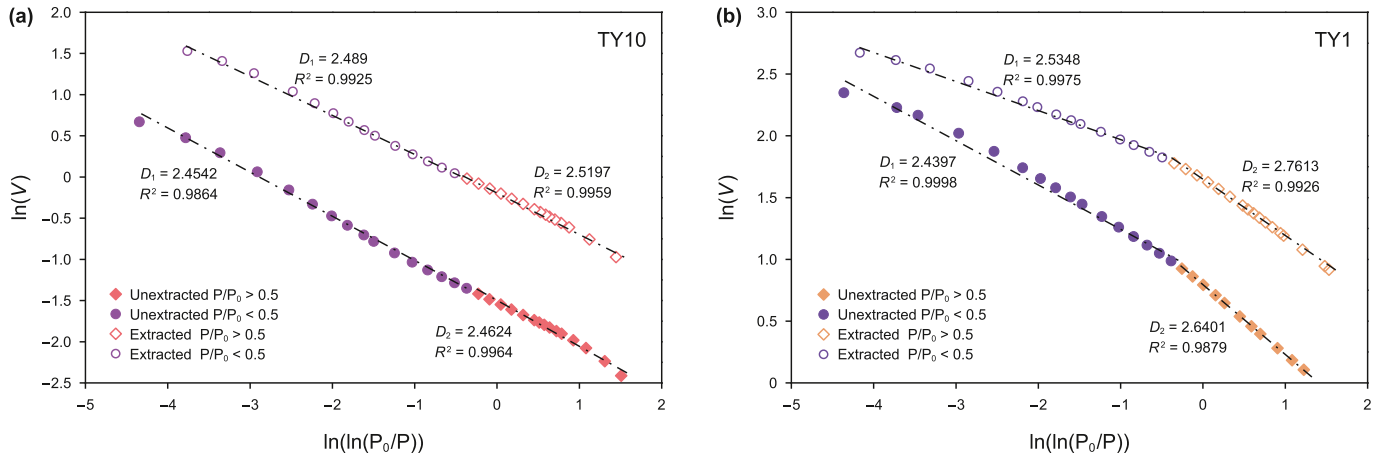


Fig. 16. Fractal calculation from nitrogen adsorption by FHH model.

Table 6  
Fractal dimensions of shales at unextracted and extracted states.

Sample	Type A or B	Unextracted				Extracted			
		$D_1$	$R^2$	$D_2$	$R^2$	$D_1$	$R^2$	$D_2$	$R^2$
TY1	B	2.4397	0.9998	2.6401	0.9879	2.5348	0.9975	2.7613	0.9926
TY2	B	2.4505	0.9994	2.6769	0.9915	2.5544	0.9979	2.7733	0.9962
TY3	B	2.4515	0.9997	2.6423	0.9930	2.5705	0.9959	2.8062	0.9932
TY4	B	2.4146	0.9995	2.6108	0.9892	2.5008	0.9989	2.7341	0.9908
TY5	B	2.4124	0.9978	2.5547	0.9823	2.5348	0.9994	2.7053	0.9835
TY6	B	2.4120	0.9923	2.6169	0.9701	2.5103	0.9998	2.7430	0.9794
TY7	B	2.4025	0.9952	2.6251	0.9795	2.4978	0.9996	2.7400	0.9882
TY8	B	2.3983	0.9976	2.6164	0.9850	2.4500	0.9991	2.6852	0.9999
TY9	B	2.4225	0.9970	2.6682	0.9708	2.5190	0.9997	2.7389	0.9704
TY10	A	2.4542	0.9864	2.4624	0.9964	2.4890	0.9925	2.5197	0.9959
TY11	A	2.4199	0.9507	2.4144	0.9969	2.5141	0.9942	2.5532	0.9926
TY12	A	2.4850	0.9910	2.4712	0.9962	2.4567	0.9948	2.5648	0.9864
TY13	A	2.4866	0.9922	2.4869	0.9982	2.5064	0.9936	2.6463	0.9633
TY14	A	2.4619	0.9083	2.4196	0.9979	2.4947	0.9938	2.6119	0.9946
TY15	B	2.4211	0.9978	2.5694	0.9844	2.5482	0.9999	2.7982	0.9837
TY16	B	2.3999	0.9965	2.6238	0.9809	2.5362	0.9997	2.7842	0.9807
TY17	A	2.4594	0.9834	2.4221	0.9937	2.4948	0.9989	2.6675	0.9919
TY18	B	2.4218	0.9996	2.6629	0.9941	2.5368	0.9993	2.8068	0.9655
TY19	A	2.4328	0.9942	2.5350	0.9973	2.5129	0.9972	2.7239	0.9965
TY20	B	2.4481	0.9993	2.7395	0.9890	2.5243	0.9973	2.7919	0.9916
TY21	A	2.4891	0.9909	2.4645	0.9982	2.5195	0.9960	2.5780	0.9988
TY22	B	2.4270	0.9995	2.7016	0.9895	2.5675	0.9986	2.8004	0.9936
TY23	B	2.4398	0.9993	2.6919	0.9931	2.5546	0.9990	2.7800	0.9967
TY24	B	2.4283	0.9993	2.7050	0.9884	2.5677	0.9987	2.8140	0.9886

shale oil content. However, organic matter acts as the principal adsorbent for shale oil, with higher organic matter content resulting in a large adsorbed oil content (including adsorbed oil, i.e., swelling oil in kerogen) (Lu et al., 2016; Li et al., 2018a).

The correlation between total shale oil content and TOC is robust ( $R^2 = 0.8933$ ), and an excellent correlation is observed between adsorbed oil and TOC with a high correlation coefficient of 0.9338, underscoring the integral role of organic matter in the adsorption of shale oil. However, the correlation between free oil and TOC is moderately positive ( $R^2 = 0.6009$ ), meaning that free oil is also influenced by pore structure in addition to organic matter (Zhang et al., 2023b). Nevertheless, a weak negative correlation between TOC and free oil ratio is observed, suggesting that an excessive organic matter content may impede the mobility of shale

oil due to the predominance of adsorbed oil. Optimal conditions for shale oil enrichment and extraction are typically found in formations with a TOC content ranging from 2% to 4%, aligning with findings from prior studies (Wang et al., 2015; Zhang et al., 2021).

### 3.4.2. Pore structures

In shale pore-fracture systems, the occurrence of shale oil is intricately governed by the pore structure. The relationships between shale oil content and pore structure parameters after extraction are plotted in Fig. 19. Adsorbed oil shows a weak negative correlation with BET SSA, and so does the total oil content (Fig. 19(a)), implying that a limited extent of the pore surfaces partake in oil adsorption within the shale matrix. And there is no clear correlation between BET SSA and free oil. As the da increases,

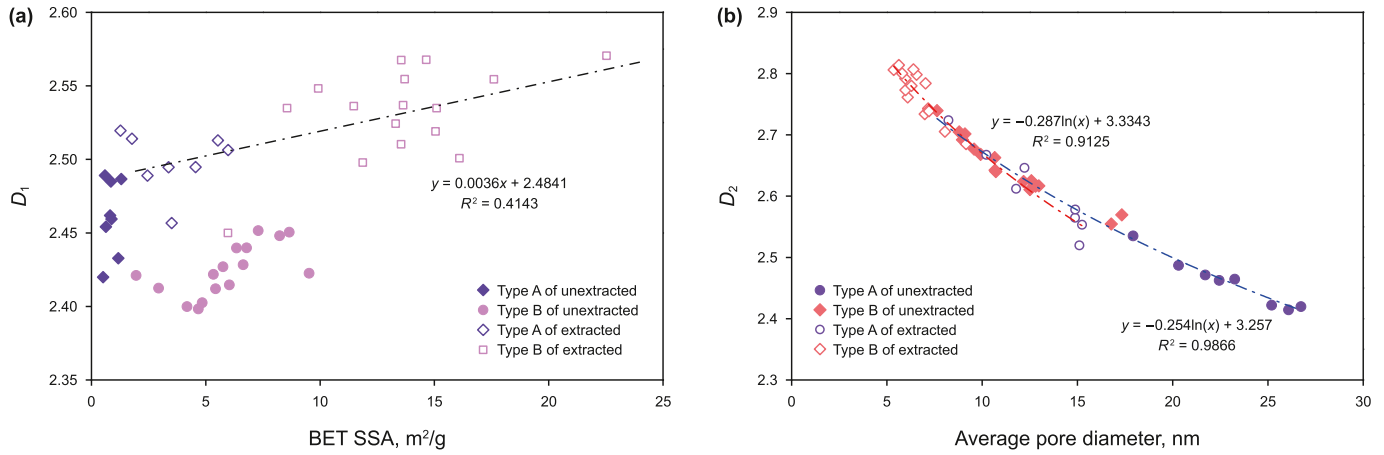


Fig. 17. Correlations between fractal dimensions and pore structure parameters.

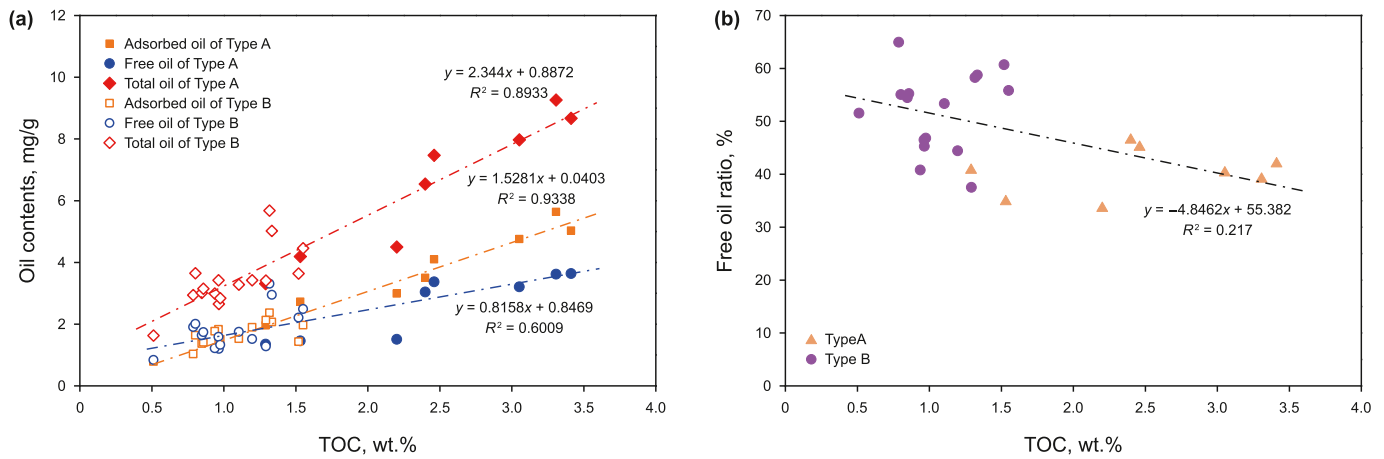


Fig. 18. Correlations between TOC and shale oil contents.

the total oil, adsorbed, and free oil contents increase (Fig. 19(b)). However, the correlation between adsorbed oil and  $d_a$  is unexpectedly stronger than that for free oil and  $d_a$ , potentially due to the  $d_a$  values from LTNA/D predominantly reflecting the pores less than 200 nm, while the free oil primarily occurs in large mesopores and macropores larger than 200 nm; on the contrary, adsorbed oil mainly exists in micropores and minipores.

Counterintuitively, the micropore volume exhibits a negative correlation with both adsorbed and total oil contents and lacks correlation with free oil, as displayed in Fig. 19(c). This pattern is echoed in the relationship between shale oil content and the volume of pores smaller than 100 nm, encompassing both micropores and minipores (Fig. 19(d)). This is because that the micropores and minipores are primarily saturated with water rather than oil, which can be proven by Fig. 20. Capillary-bound water exhibits an excellent positive correlation with BET SSA (Fig. 20(a)), suggesting that water molecules predominantly occupy the pore surfaces. The negative correlation between capillary-bound water and  $d_a$  indicates that pore water is largely confined to small nano-scale pores (Fig. 20(b)). As a result, capillary-bound water positively correlates well with micropore volume (Fig. 20(c)), as well as with the volume of pores less than 100 nm (Fig. 20(d)).

### 3.5. Pore fluid occurrence patterns in shale

As discussed, the pore fluid occurrence pattern can be inferred and depicted in Fig. 21. In shale pore-fracture systems, pore water, i.e., capillary-bound water, is predominantly confined to micropores and minipores, such as intraparticle pores in clay minerals. Adsorbed oil is localized at the interfaces of mineral particles or organic matter, as well as within the intercrystalline pores of pyrite aggregates. Notably, the pore sizes in these regions are mainly less than 100 nm. In contrast, free oil is mainly enriched in mesopores and macropores, which are primarily associated with brittle granules, such as quartz, feldspar, and calcareous minerals. Specifically, bound oil is typically found in mesopores, and macropores (including fractures) are replete with movable oil.

## 4. Conclusions

This study focused on the microscopic occurrence characteristics and controlling factors of shale oil in the Gaoyou Sag, Subei Basin, using Rock-Eval, SEM, NMR  $T_1$ – $T_2$ , and LTNA/D. The occurrence pores, states, and contents of shale oil were analyzed, and the relationships between shale oil, the abundance of organic matter, and pore structures were also discussed. The salient conclusions are summarized below.

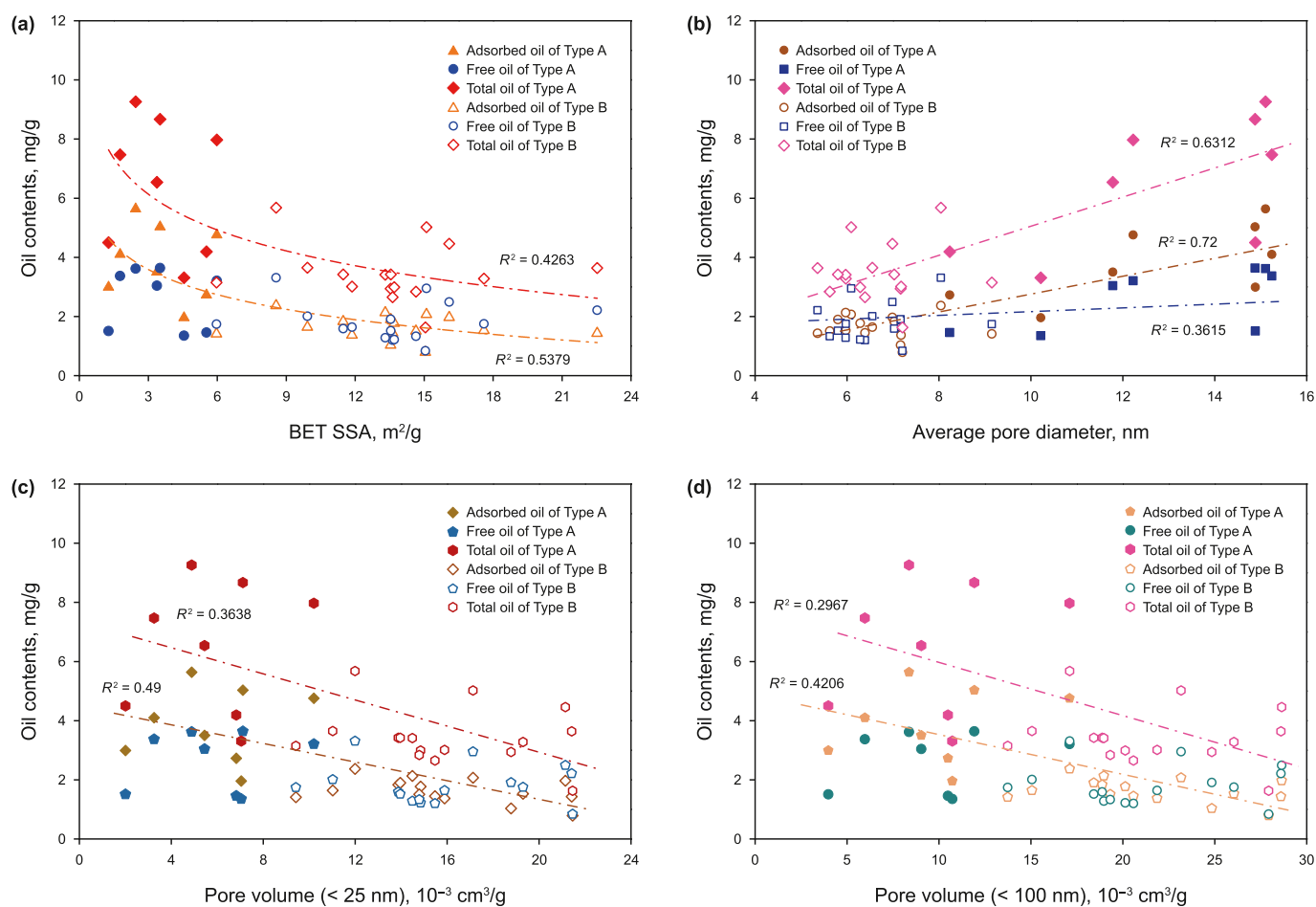


Fig. 19. Correlations between shale oil contents and pore structure parameters.

SEM imagery from the unextracted samples reveals the pore types hosting shale oil. The pore spaces predominantly consist of interparticle pores amidst brittle granules, intraparticle pores within clay mineral clusters, and fractures. Shale oil is primarily situated in fractures, with subsequent prevalence in interparticle and sizable intraparticle pores. Notably, fractures and interparticle pores linked to brittle minerals significantly facilitate the accumulation of shale oil, particularly free oil.

The nitrogen isotherms of the selected shales at unextracted and extracted states were classified into two groups. Type A shales, rich in felsic and calcareous minerals but deficient in clay minerals, are distinguished by higher contents of TOC and shale oil. Conversely, Type B shales exhibit higher clay mineral content but lower TOC and shale oil concentrations. Type A shales are deemed more favorable for shale oil enrichment and mobility, attributed to their lower BET SSA, larger da, and less complex pore surfaces and pore structures.

The organic matter abundance controls the shale oil content, while an excessive organic matter content will result in a low free oil ratio and restrict shale oil flow. The BET SSA, micropore volume, and the volume of pores less than 100 nm after extraction all associate negatively with total and adsorbed oil contents but show no correlation with free oil, while they correlate positively with capillary-bound water. In shale pore networks, pore water

primarily occupies micropores and minipores, coexisting with adsorbed oil. At the same time, mesopores and macropores are largely filled with free oil, encompassing both bound and movable oil.

#### CRediT authorship contribution statement

**Jun-jie Wang:** Writing – original draft, Methodology, Investigation, Data curation. **Peng-fei Zhang:** Writing – review & editing, Methodology, Investigation, Funding acquisition. **Shuang-fang Lu:** Writing – review & editing, Methodology, Investigation. **Zi-zhi Lin:** Methodology, Investigation, Data curation. **Wen-biao Li:** Writing – review & editing, Investigation. **Jun-jian Zhang:** Writing – review & editing, Methodology. **Wei-zheng Gao:** Data curation. **Neng-wu Zhou:** Writing – review & editing, Funding acquisition. **Guo-hui Chen:** Writing – review & editing, Methodology. **Ya-jie Yin:** Data curation. **Han Wu:** Data curation.

#### Declaration of competing interest

The authors declare that they have no known competing financial interests or personal relationships that could have appeared to influence the work reported in this paper.

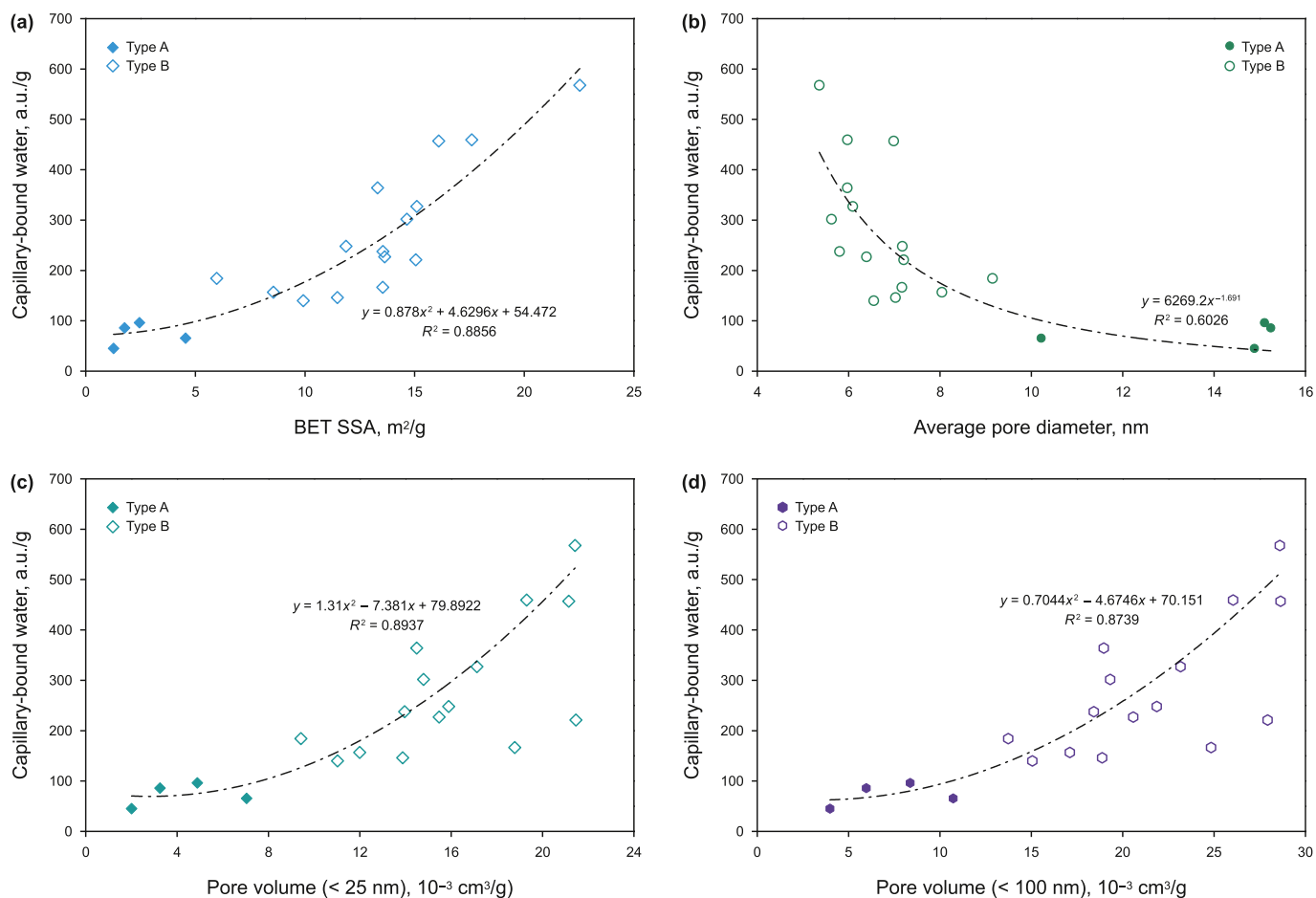


Fig. 20. Relationships between capillary-bound water and pore structure parameters.

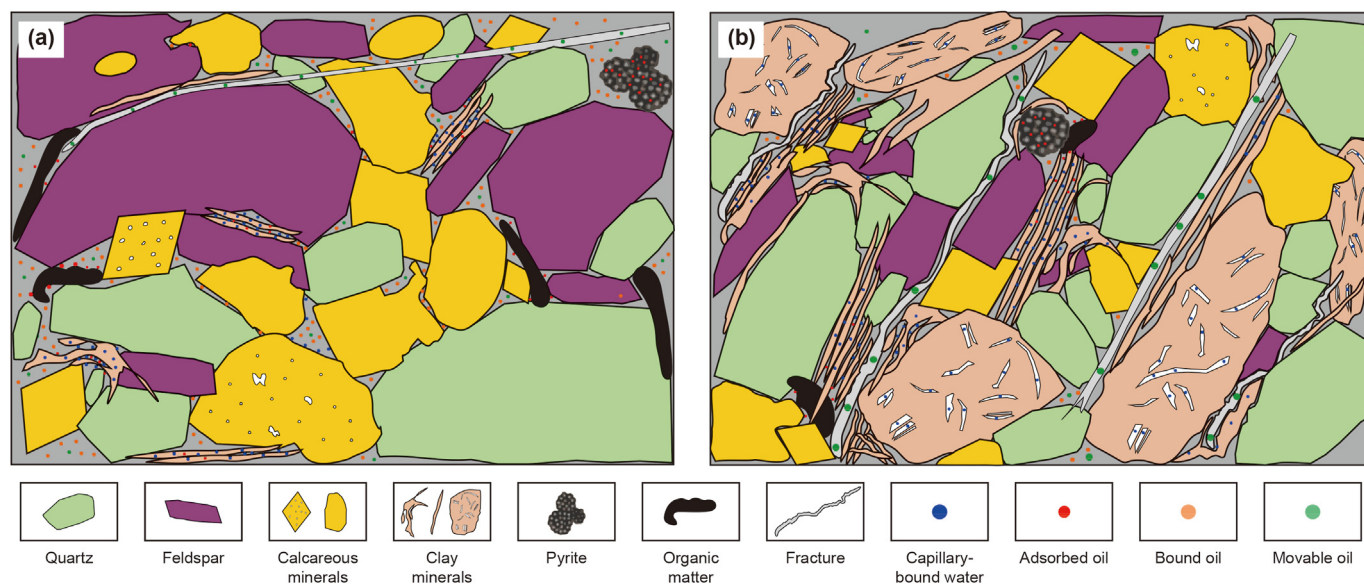


Fig. 21. Pore fluid occurrence patterns for shale oil reservoirs.

## Acknowledgments

This study was financially supported by the National Natural Science Foundation of China (42302160), the Sanya City Science and Technology Innovation Project (2022KJCS51), and the Support Plan for Outstanding Youth Innovation Team in Shandong Higher Education Institutions (2022KJ060).

## References

- Bai, L., Liu, B., Du, Y., Wang, B., Tian, S., Wang, L., Xue, Z., 2022. Distribution characteristics and oil mobility thresholds in lacustrine shale reservoir: insights from N<sub>2</sub> adsorption experiments on samples prior to and following hydrocarbon extraction. *Petrol. Sci.* 19 (2), 486–497. <https://doi.org/10.1016/j.petsci.2021.10.018>.
- Cao, T., Jiang, Q., Qian, M., Liu, P., Li, Z., Tao, G., Li, M., 2023. Key technologies for pyrolysis analysis of shale oil content. *Acta Petrol. Sin.* 44 (2), 329–338. <https://doi.org/10.7623/syxb202302008> (in Chinese).
- Dang, W., Zhang, J., Nie, H., Wang, F., Tang, X., Jiang, S., Wei, X., Liu, Q., Li, P., Li, F., Sun, J., 2022. Microscopic occurrence characteristics of shale oil and their main controlling factors: a case study of the 3rd submember continental shale of Member 7 of Yanchang Formation in Yan'an area, Ordos Basin. *Acta Petrol. Sin.* 43 (4), 507–523. <https://doi.org/10.7623/syxb202204005> (in Chinese).
- Duan, H., Liu, S., Fu, Q., 2020. Characteristics and sedimentary environment of organic-rich shale in the second member of Paleogene Funing Formation, Subei Basin. *Petrol. Geol. Exper.* 42 (4), 612–617. <https://doi.org/10.11781/sydz202004612> (in Chinese).
- Fu, Q., Liu, Q., Liu, S., Duan, H., 2020. Shale oil accumulation conditions in the second member of Paleogene Funing Formation, Gaoyou Sag, Subei Basin. *Petrol. Geol. Exper.* 42 (4), 625–631. <https://doi.org/10.11781/sydz202004625> (in Chinese).
- Guan, M., Liu, X., Jin, Z., Lai, J., Liu, J., Sun, B., Liu, T., Hua, Z., Xu, W., Shu, H., Wang, G., Liu, M., Luo, Y., 2022. Quantitative characterization of various oil contents and spatial distribution in lacustrine shales: insight from petroleum compositional characteristics derived from programmed pyrolysis. *Mar. Petrol. Geol.* 138, 105522. <https://doi.org/10.1016/j.marpetgeo.2021.105522>.
- Hu, T., Pang, X., Jiang, F., Wang, Q., Liu, X., Wang, Z., Jiang, S., Wu, G., Li, G., Xu, T., Li, M., Yu, J., Zhang, C., 2021. Movable oil content evaluation of lacustrine organic-rich shales: methods and a novel quantitative evaluation model. *Earth Sci. Rev.* 214, 103545. <https://doi.org/10.1016/j.earscirev.2021.103545>.
- Jarvie, D.M., 2012. Shale resource systems for oil and gas; Part 2. Shale-oil resource systems. *AAPG Mem* 97, 89–119. <https://doi.org/10.1306/13321447M973489>.
- Jiang, Q., Li, M., Qian, M., Li, Z., Li, Z., Huang, Z., Zhang, C., Ma, Y., 2016. Quantitative characterization of shale oil in different occurrence states and its application. *Petrol. Geol. Exper.* 38 (6), 842–849. <https://doi.org/10.11781/sydz201606842> (in Chinese).
- Jin, Z., Zhang, Q., Zhu, R., Dong, L., Fu, J., Liu, H., Yun, L., Liu, G., Li, M., Zhao, X., Wang, X., Hu, S., Tang, Y., Bai, Z., Sun, D., Li, X., 2023. Classification of lacustrine shale oil reservoirs in China and its significance. *Oil Gas Geol.* 44 (4), 801–819. <https://doi.org/10.11743/ogg20230401> (in Chinese).
- Li, A., Ding, W., He, J., Dai, P., Yin, S., Xie, F., 2016. Investigation of pore structure and fractal characteristics of organic-rich shale reservoirs: a case study of Lower Cambrian Qiongzhusi formation in Malong block of eastern Yunnan Province, South China. *Mar. Petrol. Geol.* 70, 46–57. <https://doi.org/10.1016/j.marpetgeo.2015.11.004>.
- Li, C., Tan, M., Wang, Z., Li, Y., Xiao, L., 2023. Nuclear magnetic resonance pore radius transformation method and fluid mobility characterization of shale oil reservoirs. *Geoenergy Sci. Eng.* 221, 211403. <https://doi.org/10.1016/j.jgeoen.2022.211403>.
- Li, J., Lu, S., Xie, L., Zhang, J., Xue, H., Zhang, P., Tian, S., 2017. Modeling of hydrocarbon adsorption on continental oil shale: a case study on n-alkane. *Fuel* 206, 603–613. <https://doi.org/10.1016/j.fuel.2017.06.017>.
- Li, J., Lu, S., Cai, J., Zhang, P., Xue, H., Zhao, X., 2018a. Adsorbed and free oil in lacustrine nanoporous shale: a theoretical model and a case study. *Energ. Fuel* 32 (12), 12247–12258. <https://doi.org/10.1021/acs.energyfuels.8b02953>.
- Li, J., Song, Z., Wang, M., Zhang, P., Cai, J., 2024. Quantitative characterization of microscopic occurrence and mobility of oil in shale matrix pores: a case study of the Shahejie Formation in the Dongying Sag. *Petrol. Sci. Bull.* 1, 1–20. <https://doi.org/10.3969/j.issn.2096-1693.2024.01.001> (in Chinese).
- Li, J., Huang, W., Lu, S., Wang, M., Chen, G., Tian, W., Guo, Z., 2018b. Nuclear magnetic resonance T<sub>1</sub>–T<sub>2</sub> Map Division method for hydrogen-bearing components in continental shale. *Energ. Fuel* 32 (9), 9043–9054. <https://doi.org/10.1021/acs.energyfuels.8b01541>.
- Li, J., Jiang, C., Wang, M., Lu, S., Chen, Z., Chen, G., Li, J., Li, Z., Lu, S., 2020b. Adsorbed and free hydrocarbons in unconventional shale reservoir: a new insight from NMR T<sub>1</sub>–T<sub>2</sub> maps. *Mar. Petrol. Geol.* 116, 104311. <https://doi.org/10.1016/j.marpetgeo.2020.104311>.
- Li, J., Wang, M., Fei, J., Xu, L., Shao, H., Li, M., Tian, W., Lu, S., 2022a. Determination of in situ hydrocarbon contents in shale oil plays. Part 2: two-dimensional nuclear magnetic resonance (2D NMR) as a potential approach to characterize preserved cores. *Mar. Petrol. Geol.* 145, 105890. <https://doi.org/10.1016/j.marpetgeo.2022.105890>.
- Li, J., Wang, M., Jiang, C., Lu, S., Li, Z., 2022b. Sorption model of lacustrine shale oil: insights from the contribution of organic matter and clay minerals. *Energy* 260, 125011. <https://doi.org/10.1016/j.energy.2022.125011>.
- Li, J., Yin, J., Zhang, Y., Lu, S., Wang, W., Li, J., Chen, F., Meng, Y., 2015a. A comparison of experimental methods for describing shale pore features — a case study in the Bohai Bay Basin of eastern China. *Int. J. Coal Geol.* 152, 39–49. <https://doi.org/10.1016/j.coal.2015.10.009>.
- Li, W., Lu, S., Xue, H., Zhang, P., Hu, Y., 2015b. Oil content in argillaceous dolomite from the Jiangnan Basin, China: application of new grading evaluation criteria to study shale oil potential. *Fuel* 143, 424–429. <https://doi.org/10.1016/j.fuel.2014.11.080>.
- Li, W., Cao, J., Shi, C., Xu, T., Zhang, H., Zhang, Y., 2020a. Shale oil in saline lacustrine systems: a perspective of complex lithologies of fine-grained rocks. *Mar. Petrol. Geol.* 116, 104351. <https://doi.org/10.1016/j.marpetgeo.2020.104351>.
- Liang, C., Wu, J., Cao, Y., Liu, K., Khan, D., 2022. Storage space development and hydrocarbon occurrence model controlled by lithofacies in the Eocene Jiyang Sub-basin, East China: significance for shale oil reservoir formation. *J. Petrol. Sci. Eng.* 215, 110631. <https://doi.org/10.1016/j.petrol.2022.110631>.
- Lin, Z., Li, J., Lu, S., Hu, Q., Zhang, P., Wang, J., Zhi, Q., Huang, H., Yin, N., Wang, Y., Ge, T., 2024. The occurrence characteristics of oil in shales matrix from organic geochemical screening data and pore structure properties: an experimental study. *Petrol. Sci.* 21 (1), 1–13. <https://doi.org/10.1016/j.petsci.2023.09.002>.
- Liu, B., Bai, L., Chi, Y., Jia, R., Fu, X., Yang, L., 2019. Geochemical characterization and quantitative evaluation of shale oil reservoir by two-dimensional nuclear magnetic resonance and quantitative grain fluorescence on extract: a case study from the Qingshankou Formation in Southern Songliao Basin, northeast China. *Mar. Petrol. Geol.* 109, 561–573. <https://doi.org/10.1016/j.marpetgeo.2019.06.046>.
- Liu, B., Jiang, X., Bai, L., Lu, R., 2022. Investigation of oil and water migrations in lacustrine oil shales using 20 MHz 2D NMR relaxometry techniques. *Petrol. Sci.* 19 (3), 1007–1018. <https://doi.org/10.1016/j.petsci.2021.10.011>.
- Liu, X., Lai, J., Fan, X., Shu, H., Wang, G., Ma, X., Liu, M., Guan, M., Luo, F., 2020. Insights in the pore structure, fluid mobility and oiliness in oil shales of Paleogene Funing Formation in Subei Basin, China. *Mar. Petrol. Geol.* 114, 104228. <https://doi.org/10.1016/j.marpetgeo.2020.104228>.
- Lu, S., Huang, W., Chen, F., Li, J., Wang, M., Xue, H., Wang, W., Cai, X., 2012. Classification and evaluation criteria of shale oil and gas resources: Discussion and application. *Petrol. Explor. Develop.* 39 (2), 268–276. [https://doi.org/10.1016/S1876-3804\(12\)60042-1](https://doi.org/10.1016/S1876-3804(12)60042-1).
- Lu, S., Xue, H., Wang, M., Xiao, D., Huang, W., Li, J., Xie, L., Tian, S., Wang, S., Li, J., Wang, W., Chen, F., Li, W., Xue, Q., Liu, X., 2016. Several key issues and research trends in evaluation of shale oil. *Acta Petrol. Sin.* 37 (10), 1309–1322. <https://doi.org/10.7623/syxb201610012> (in Chinese).
- Ma, C., Zhao, X., Yang, T., Jiang, W., Guo, B., Han, G., Bi, H., Ma, J., Bian, C., Zhou, K., Zhou, S., Zhu, H., 2022. Mineralogy, organic geochemistry, and microstructural characterization of lacustrine Shahejie Formation, Qikou Sag, Bohai Bay Basin: contribution to understanding microcosmic storage mechanism of shale oil. *J. Petrol. Sci. Eng.* 209, 109843. <https://doi.org/10.1016/j.petrol.2021.109843>.
- Mei, Q., Guo, R., Zhou, X., Cheng, G., Li, S., Bai, Y., Liu, J., Wu, W., Zhao, J., 2023. Pore structure characteristics and impact factors of laminated shale oil reservoir in Chang 73 sub-member of Ordos Basin, China. *J. Nat. Gas Geosci.* 8 (4), 227–243. <https://doi.org/10.1016/j.jnggs.2023.07.003>.
- Wang, J., Lu, S., Zhang, P., Li, Q., Yin, Y., Li, W., Zhou, N., Chen, G., Yi, Y., Wu, C., 2024. Characterization of shale oil and water micro-occurrence based on a novel method for fluid identification by NMR T<sub>2</sub> spectrum. *Fuel* 374, 132426. <https://doi.org/10.1016/j.fuel.2024.132426>.
- Wang, M., Xue, H., Tian, S., Wilkins, R., Wang, Z., 2015. Fractal characteristics of Upper Cretaceous lacustrine shale from the Songliao basin, NE China. *Mar. Petrol. Geol.* 67, 144–153. <https://doi.org/10.1016/j.marpetgeo.2015.05.011>.
- Wang, M., Ma, R., Li, J., Lu, S., Li, C., Guo, Z., Li, Z., 2019. Occurrence mechanism of lacustrine shale oil in the Paleogene Shahejie formation of Jiyang depression, Bohai Bay Basin, China. *Petrol. Explor. Develop.* 46 (4), 833–846. [https://doi.org/10.1016/S1876-3804\(19\)60242-9](https://doi.org/10.1016/S1876-3804(19)60242-9).
- Wang, M., Li, M., Li, J., Xu, L., Zhang, J., 2022a. The key parameter of shale oil resource evaluation: oil content. *Petrol. Sci.* 19 (4), 1443–1459. <https://doi.org/10.1016/j.petsci.2022.03.006>.
- Wang, N., Li, C., Feng, Y., Song, Y., Guo, T., Li, M., Chen, Z., 2022b. Novel method for determining the oil moveable threshold and an innovative model for evaluating the oil content in shales. *Energy* 239, 121484. <https://doi.org/10.1016/j.energy.2021.121484>.
- Wang, X., Wang, M., Li, J., Shao, H., Deng, Z., Wu, Y., 2022c. Thermal maturity: the controlling factor of wettability, pore structure, and oil content in the lacustrine Qingshankou shale, Songliao Basin. *J. Petrol. Sci. Eng.* 215, 110648. <https://doi.org/10.1016/j.petrol.2022.110648>.
- Wang, Y., Zhu, Y., Liu, S., Zhang, R., 2016. Pore characterization and its impact on methane adsorption capacity for organic-rich marine shales. *Fuel* 181, 227–237. <https://doi.org/10.1016/j.fuel.2016.04.082>.
- Xue, H., Tian, S., Wang, W., Zhang, W., Du, T., Mu, G., 2016. Correction of oil content—One key parameter in shale oil resource assessment. *Oil Gas Geol.* 37 (1), 15–22. <https://doi.org/10.11743/ogg20160103> (in Chinese).
- Yao, Y., Liu, D., Tang, D., Tang, S., Huang, W., 2008. Fractal characterization of adsorption-pores of coals from North China: an investigation on CH<sub>4</sub> adsorption capacity of coals. *Int. J. Coal Geol.* 73 (1), 27–42. <https://doi.org/10.1016/j.coal.2007.07.003>.
- Zan, 2020. Enrichment characteristics and main controlling factors of shale oil reservoir in the second member of Paleogene Funing Formation, Beigang

- Subsag, Jinhu Sag, Subei Basin. *Petrol. Geol. Exper.* 42 (4), 618–624. <https://doi.org/10.11781/sysydz202004618> (in Chinese).
- Zhang, H., Huang, H., Li, Z., Liu, M., 2019. Comparative study between sequential solvent-extraction and multiple isothermal stages pyrolysis: a case study on Eocene Shahejie Formation shales, Dongying Depression, East China. *Fuel* 263, 116591. <https://doi.org/10.1016/j.fuel.2019.116591>.
- Zhang, J., Zhu, R., Wu, S., Jiang, X., Liu, C., Cai, Y., Zhang, S., Zhang, S., 2023a. Microscopic oil occurrence in high-maturity lacustrine shales: Qingshankou Formation, Gulong Sag, Songliao basin. *Petrol. Sci.* 20 (5), 2726–2746. <https://doi.org/10.1016/j.petsci.2023.08.026>.
- Zhang, P., Lu, S., Li, J., Xue, H., Li, W., Zhang, P., 2017. Characterization of shale pore system: a case study of Paleogene Xin'gouzui Formation in the Jianghan basin, China. *Mar. Petrol. Geol.* 79, 321–334. <https://doi.org/10.1016/j.marpetgeo.2016.10.014>.
- Zhang, P., Lu, S., Li, J., Chen, C., Xue, H., Zhang, J., 2018. Petrophysical characterization of oil-bearing shales by low-field nuclear magnetic resonance (NMR). *Mar. Petrol. Geol.* 89, 778–785. <https://doi.org/10.1016/j.marpetgeo.2017.11.015>.
- Zhang, P., Lu, S., Li, J., Chang, X., 2020. 1D and 2D Nuclear magnetic resonance (NMR) relaxation behaviors of protons in clay, kerogen and oil-bearing shale rocks. *Mar. Petrol. Geol.* 114, 104210. <https://doi.org/10.1016/j.marpetgeo.2019.104210>.
- Zhang, P., Lu, S., Zeng, Z., Chang, X., Li, J., Chen, G., Zhang, J., Lin, Z., Li, J., 2021. Pore structure and fractal character of lacustrine oil-bearing shale from the Dongying Sag, Bohai Bay Basin, China. *Geofluids* 1–19. <https://doi.org/10.1155/2021/9945494>.
- Zhang, P., Lu, S., Li, J., Chang, X., Lin, Z., Chen, G., Li, J., Liu, J., Tian, S., 2022a. Evaluating microdistribution of adsorbed and free oil in a lacustrine shale using nuclear magnetic resonance: a theoretical and experimental study. *J. Petrol. Sci. Eng.* 212, 110208. <https://doi.org/10.1016/j.petrol.2022.110208>.
- Zhang, P., Lu, S., Li, Z., Duan, H., Chang, X., Qiu, Y., Fu, Q., Zhi, Q., Wang, J., Huang, H., 2022b. Key oil content parameter Correction of shale oil resources: a case study of the Paleogene Funing Formation, Subei Basin, China. *Energy. Fuel.* 36 (10), 5316–5326. <https://doi.org/10.1021/acs.energyfuels.2c00610>.
- Zhang, P., Lu, S., Li, J., Wang, J., Zhang, J., 2023b. Oil occurrence mechanism in nanoporous shales: a theoretical and experimental study. *Mar. Petrol. Geol.* 156, 106442. <https://doi.org/10.1016/j.marpetgeo.2023.106442>.
- Zhang, P., Yin, Y., Lu, S., Wang, J., Zhang, J., Zhi, Q., Huang, H., 2023c. Key factors controlling oil contents in different lithofacies shales from the Funing Formation, Subei Basin: Evidence from scanning electron microscopy. *Mar. Petrol. Geol.* 229, 212115. <https://doi.org/10.1016/j.marpetgeo.2023.212115>.
- Zhang, P., Lu, S., Wang, J., Li, W., Yin, Y., Chen, G., Zhou, N., Wu, H., 2024a. Microscopic occurrence and distribution of oil and water in situ shale: Evidence from nuclear magnetic resonance. *Petrol. Sci.* <https://doi.org/10.1016/j.petsci.2024.04.007>.
- Zhang, P., Wu, H., Lu, S., Wang, J., Li, W., Yin, Y., Zhou, N., Zhang, J., Chen, G., Yi, Y., Wu, C., 2024b. The occurrence of pore fluid in shale-oil reservoirs using nuclear magnetic resonance: the Paleogene Funing Formation, Subei Basin, Eastern China. *Mar. Petrol. Geol.* 167, 106986. <https://doi.org/10.1016/j.marpetgeo.2024.106986>.
- Zhang, Q., Jin, Z., Zhu, R., Liu, Q., Zhang, R., Wang, G., Chen, W., Littke, R., 2023d. Remarkable issues of Rock-Eval pyrolysis in the assessment of shale oil/gas. *Oil Gas Geol.* 44 (4), 1020–1032. <https://doi.org/10.11743/ogg20230417> (in Chinese).
- Zhu, X., Duan, H., Sun, Y., 2023. Breakthrough and significance of Paleogene continental shale oil exploration in Gaoyou Sag, Subei Basin. *Acta Petrol. Sin.* 44 (8), 1206–1221+1257. <https://doi.org/10.7623/syxb202308002> (in Chinese).
- Zou, C., Yang, Z., Cui, J., Zhu, R., Hou, L., Tao, S., Yuan, X., Wu, S., Lin, S., Wang, L., Bai, B., Yao, J., 2013. Formation mechanism, geological characteristics and development strategy of nonmarine shale oil in China. *Petrol. Explor. Develop.* 40 (1), 15–27. [https://doi.org/10.1016/S1876-3804\(13\)60002-6](https://doi.org/10.1016/S1876-3804(13)60002-6).
- Zou, C., Pan, S., Jing, Z., Gao, J., Yang, Z., Wu, S., Zhao, Q., 2020. Shale oil and gas revolution and its impact. *Acta Petrol. Sin.* 41 (1), 1–12. <https://doi.org/10.7623/syxb202001001> (in Chinese).